QUANTUM COMPUTING OVER LONG TIME SCALES IN A SINGLY CHARGED QUANTUM DOT

by

Bo Sun

A dissertation submitted in partial fulfillment
of the requirements for the degree of
Doctor of Philosophy
(Applied Physics)
in The University of Michigan
2011

Doctoral Commitee:

Professor Duncan G. Steel, Chair
Professor Paul R. Berman
Assistant Professor Hui Deng
Assistant Professor Vanessa Sih

ACKNOWLEDGEMENTS

I'd first like to thank my parents for their support and encouragement over the many years. Their perseverance over the many hardships that they have had to faces have inspired me to meet my own challenges head on. I'd like to thank my wonderful girlfriend Kristi for giving me a new perspective on life and for maintaining my mental health. Of all my graduate student friends working in the many labs throughout the university, I truly think that my experience has been the best and most fruitful. Duncan's commitment to his students and his genuine care for our education and well being has created a environment where I felt at home and where I could really endeavor to do research at the forefront of science. I am humbled and privileged to have worked under Xiaodong, who taught me how to do research. He was keen to teach and gave me phenomenal opportunities. Xiaodong and Duncan are my exemplars of hard work and I hope to someday to mimic their drive, energy, and focus. I really have to thank Yanwen for telling it like it was, taking me aside and saying that I was "being a brat." This really changed my attitude toward research early on, and really made me more aware of all the things which I did not know and had yet to learn. Katherine and Leon have been wonderful friends in and out of the lab and have really enriched my time here in Ann Arbor. Colin and Renee are great to work with and I know that they will do great in the lab. While I didn't work on the same experiment as John, Alex, Vasudev, and Meredith, I loved to hear about the exciting results that they have seen as well as the confounding problems that have confronted them. My labmates have really been the most brilliant group of people that I have had the pleasure of working with. Of course, I have to give John extra

credit for being the only one to edit my thesis.

TABLE OF CONTENTS

LIST OF FIGURES

LIST OF APPENDICES

Appendix

CHAPTER 1

Introduction

By exploiting the properties of coherent quantum mechanical systems and the superposition of quantum states, quantum computing and information processing can efficiently solve a number of computation problems that may otherwise be too slow to solve on a classical computer. Some famous examples include the simulation of quantum mechanical systems [1–3], factoring large numbers [4], or searching a large database [5]. Of particular interest is the ability to use Shor's algorithm [4] to factor large numbers, as this has a direct impact on the security of public key cryptography.

Public key cryptography solves the basic key distribution problem affecting all encryption schemes by using a set of public and private encryption keys. While the public key is readily available to all and can be used to encrypt data quickly, it becomes computationally difficult to decrypt the information without the private key. This is possible due to the mathematical relationship between the public and private keys and the encryption methodology and involves the use of so called asymmetric or one-way algorithms. For example, while finding and multiplying two large numbers is computationally easy, factoring a large number into its prime factors is computationally difficult. Various implementations of public key cryptography are used to secure computer networks and computer information transactions on both public internet sites and private, government, or military intranets. Peter Shor's algorithm renders all current public key encryption methods vulnerable to attack by allowing the efficient solution of prime factorization and the computation of discrete logarithms. Thus, quantum computing has caught the attention of government agencies worldwide.

In 2000, David DiVincenzo proposed five criteria for practical quantum computers. They should (1) be a scalable physical system with well defined qubits. (2) have the ability to initialize all qubits to a simple fiducial state such as $|0000...\rangle$ (3) have long coherence times, much longer than the gate operation time (4) have a universal set of quantum gates (5) have the ability to measure a specific qubit. While trapped ions [6], superconductors [7], and nitrogen vacancy centers in diamonds [8,9] are just some of the many such systems currently under investigation, our laboratory is interested in quantum computing in semiconductor quantum dots.

Semiconductors are a natural system for quantum computing, as it is a scalable system with a large industrial base. Furthermore, direct bandgap semiconductors such as GaAs potentially allow the use of ultrafast laser pulses to enable fast gate operations. However, whereas the physics of resonant or nearly resonant optical interaction with atoms is well understood and ultrafast coherent optical manipulation of the atomic states can be performed through methods such as Rabi oscillation, stimulated Raman transitions, rapid adiabatic passage, etc. [10], the extended nature of the electronic wavefunctions in condensed matter systems makes such methods far more complicated and leads to such manybody effects such as exciton-exciton interaction through Coulomb coupling, exchange interactions, and screening [11–13].

Instead, by confining the electron wavefunction in a quantum dot, the three dimensional confinement potential can lift the degeneracy of the many-exciton states and recovery the atom-like delta-function density of states and greatly simplifies the physics of the light matter interaction. Over the last two decades there has been much progress in this area and there have been many advances toward quantum computation in semiconductor quantum dots made by numerous research groups around the world. For example, high spatial resolution optical spectroscopy has allowed the study of single quantum dots [14–20]. This lifts the inhomogeous broadening of the ensemble and allows the observation of spectrally sharp effects such as exchange splitting [21,22] and nuclear spin interactions [23]. Additionally, photon antibunching experiments [24,25] have confirm the ability to study single dots and the quantum nature of the dot transitions. This opens the door to quantum dot based single photon

emitters, useful for quantum key distribution methods.

1.1 Review

Over the years, we have achieved a number of important milestones in our pursuit of quantum computing in quantum dots. In this section, I will give a brief review of the experiments performed in our laboratory.

1.1.1 Isolated Single Excitons in Interface Fluctuation Quantum Dots

As was previously mentioned, the confinement of the electron wavefunction in the quantum dot avoids the complications of manybody physics by eliminating exciton-exciton interactions. Work by Bonadeo et al on single interface fluctuation quantum dots (IFQD) [1] shows that excitons are indeed isolated from manybody effects. Using differential transmission technique, where a pump and probe laser are chopped at two frequencies and the signal is measured at the difference frequency, measurements of the third order susceptibility [26] show the "single atom"-like nature of the exciton transitions in a single quantum dot. The nonlinear response showed no interaction between excitons in separate dots and there was no line broadening or frequency shifts seen in higher dimensional systems [11–13]. When the pump and probe lasers were nearly degenerate, differential transmission spectrum of the probe absorption did not exhibit peaks associated with pure dephasing. The exciton is homogeneously broadened and behaves as a single two level system where the dephasing is primarily due to relaxation. The exciton states are well defined and can possibly serve as the physical basis for the qubit.

1.1.2 Coherence of the Optical Dipole and Rabi Oscillations in Quantum Dots

The next step along the path toward quantum computation is to use optical pulses

---

[1]The quantum dots are formed by the monolayer fluctuations at the interface between a quantum well and bulk semiconductor

to generate and control coherence of the exciton transition. By using two pulsed optical fields, Bonadeo et al measured the coherence of the optical dipole of one of the exciton states [27]. The first pulse creates an optical coherence and a second pulse will interfere with that coherence either constructively or destructively depending on the delay between the two pulses. This results in a optical fringe pattern as a function of delay that decays in time. This decay is a measure of the optical decoherence time, T2, and was found to be about 40ps.

Rabi oscillations are important phenomenon in strong field interactions. When the optical field is large so that the Rabi frequency ($\Omega_r \equiv \frac{\mu E}{\hbar}$ where μ is the optical dipole moment and E is electric field) is large compared to the resonance linewidth, the light field drives coherent oscillations of the population between the ground and excited states of a two level system. The presence of such oscillations show that the QD maintains its atom like behavior even under intense optical pumping. Moreover, Rabi oscillations can act as a qubit rotation. Rabi oscillation of the exciton transition in a single IFQD was first detected using differential transmission by Stievater et al [28] by pumping on one exciton transition while probing the second. This work was later extended to biexcitons by Li et al [29].

1.1.3   Raman Coherence in Single Quantum Dots

Using broadband optical pulses which couple both the exciton transitions, it is possible to generate coherence between the two exciton states[2]. Bonadeo et al [27] demonstrated the generation of this coherence and the manipulation of the superposition wavefunction by controlling the optical phase between two excitation pulses. As the optical phase varies on a femtosecond timescale, this is an ultrafast method of qubit coherent control

Dutt et al [30] has achieved the same type of coherent control but in an ensemble of charged IFQDs where electron spin captured inside the dots can be the basis for the qubit. When a magnetic field is applied in the Voigt geometry (perpendicular to

---

[2]see Chapter 3 for information on the anisotropically split exciton states.

the growth axis), the ground spin states are split and the spin flip Raman transitions are turned on. An optical pulse can act on this Raman transition and generate spin coherence. In a method analogous to the neutral quantum dot, two pulses can be used to control the spin on an ultrafast timescale by varying the optical phase between the two pulses.

1.1.4   Biexciton Entanglement in a Single Interface Fluctuation Quatnum Dot

It is also possible to generate two excitons in a single IFQD. The four level diamond system of the biexciton system can be used as a two qubit system with each of the four states representing one of the two-qubit states ($|00\rangle$, $|01\rangle$, $|10\rangle$, $|11\rangle$). Due to Coulomb coupling, the exciton-biexciton transition is lower in energy than the ground state - exciton transition. Chen et al [31,32] demonstrated that using two non-degenerate fields to simultaneously excite the ground-exciton and exciton-biexciton transisions, it is possible to detect coherent interaction between two fields. These two continuous wave (CW) fields can also generate entanglement of the two excitons, identified through spectral features of the absorption spectrum. This work was later extended by Li et al [33] using pulsed lasers to generate two-qubit controlled-rotation and controlled-not gates.

1.1.5   Spin Rabi Oscillation, Coherent Control and Phase Gates with a Single Electron in a Self Assembled Quantum Dot

The latest work in our laboratory is in single, charged self assembled quantum dots. We will describe these dots later in Chapter 2 and the continuous wave spectroscopy of these dots is the focus of this thesis. In addition to CW spectroscopy, there have been many experimental accomplishments in the time domain. By applying a magnetic field in the Voigt profile (as with the IFQD), the electron spin states are split and the spin flip Raman transitions are turned on (see Chapter 3). Using detuned optical pulses, Kim et al [34] have demonstrated coherent control of a single electron in a

single SAQD. The detuned pulses act act only on the two photon resonance and generate minimal excited state population while creating spin Rabi oscillations. A single spin qubit phase gate has also been demonstrated by applying a strong CW beam which applies a geometric phase to one of the spin states.

1.2 Thesis Outline

In this thesis, I will discuss some of the results of CW spectroscopy of single neutral and singly charged SAQDs. First, Chapter 2 will give a brief overview of the sample structure, the relevant condensed matter physics, and the experimental methods used in this thesis. Chapter 3 will then describe the two types of three level systems found in neutral and charged quantum dots. The V-system is used to probe the dot for deviations from atomic theory, while the Λ system can be used to manipulate and measure the electron spin coherence. In Chapters 4 and 5, we will describe new physics, an interaction between the hole spin and the background nuclear spins which lead to a feedback mechanism that can suppress electron spin dephasing. Finally, we will review the experiments in this thesis and talk about possible future direction in Chapter 6.

BIBLIOGRAPHY

BIBLIOGRAPHY

[1] R. P. Feynman, "Simulating physics with computers", *International Journal of Theoretical Physics* **21**, 467 (1982).

[2] D. Deutsch, "Quantum Theory, the Church-Turing Principle and the Universal Quantum Computer", *Proceedings of the Royal Society of London. A. Mathematical and Physical Sciences* **400**, 97 (1985).

[3] S. Lloyd, "Universal Quantum Simulators", *Science* **273**, 1073 (1996).

[4] P. W. Shor, "Polynomial-Time Algorithms for Prime Factorization and Discrete Logarithms on a Quantum Computer", *SIAM Review* **41**, 303 (1999).

[5] L. K. Grover, "A fast quantum mechanical algorithm for database search", *quant-ph/9605043* (1996).

[6] C. Monroe, "Quantum information processing with atoms and photons", *Nature* **416**, 238 (2002).

[7] A. Wallraff, D. I. Schuster, A. Blais, L. Frunzio, R.-S. Huang, J. Majer, S. Kumar, S. M. Girvin, R. J. Schoelkopf, "Strong coupling of a single photon to a superconducting qubit using circuit quantum electrodynamics", *Nature* **431**, 162 (2004).

[8] M. V. G. Dutt, L. Childress, L. Jiang, E. Togan, J. Maze, F. Jelezko, A. S. Zibrov, P. R. Hemmer, M. D. Lukin, "Quantum Register Based on Individual Electronic and Nuclear Spin Qubits in Diamond", *Science* **316**, 1312 (2007).

[9] D. D. Awschalom, R. Epstein, R. Hanson, "The Diamond Age Diamond Age of Spintronics", *Scientific American* **297**, 84 (2007).

[10] P. R. Berman, V. S. Malinovsky, *Principles of Laser Spectroscopy and Quantum Optics*, Princeton University Press, ISBN 0691140561 (2010).

[11] H. Haug, *Quantum theory of the optical and electronic properties of semiconductors*, World Scientific, Singapore ;;River Edge NJ, 2nd ed. edition, ISBN 9789810213411 (1993).

[12] S. Schmitt-Rink, D. S. Chemla, D. A. B. Miller, "Linear and nonlinear optical properties of semiconductor quantum wells", *Advances in Physics* **38**, 89 (1989).

[13] H. Wang, K. Ferrio, D. G. Steel, Y. Z. Hu, R. Binder, S. W. Koch, "Transient nonlinear optical response from excitation induced dephasing in GaAs", *Physical Review Letters* **71**, 1261 (1993).

[14] H. F. Hess, E. Betzig, T. D. Harris, L. N. Pfeiffer, K. W. West, "Near-Field Spectroscopy of the Quantum Constituents of a Luminescent System", *Science* **264**, 1740 (1994).

[15] D. Gammon, E. S. Snow, D. S. Katzer, "Excited state spectroscopy of excitons in single quantum dots", *Applied Physics Letters* **67**, 2391 (1995).

[16] D. Gammon, E. S. Snow, B. V. Shanabrook, D. S. Katzer, D. Park, "Homogeneous Linewidths in the Optical Spectrum of a Single Gallium Arsenide Quantum Dot", *Science* **273**, 87 (1996).

[17] K. Brunner, G. Abstreiter, G. Bohm, G. Trankle, G. Weimann, "Sharp-line photoluminescence of excitons localized at GaAs/AlGaAs quantum well inhomogeneities", *Applied Physics Letters* **64**, 3320 (1994).

[18] J. Y. Marzin, J. M. Grard, A. Izral, D. Barrier, G. Bastard, "Photoluminescence of Single InAs Quantum Dots Obtained by Self-Organized Growth on GaAs", *Physical Review Letters* **73**, 716 (1994).

[19] M. Grundmann, J. Christen, N. N. Ledentsov, J. Bhrer, D. Bimberg, d. d. Ruvimov, P. Werner, U. Richter, U. Gsele, J. Heydenreich, V. M. Ustinov, A. Y. Egorov, A. E. Zhukov, P. S. Kop'ev, Z. I. Alferov, "Ultranarrow Luminescence Lines from Single Quantum Dots", *Physical Review Letters* **74**, 4043 (1995).

[20] J. R. Guest, T. H. Stievater, X. Li, J. Cheng, D. G. Steel, D. Gammon, D. S. Katzer, D. Park, C. Ell, A. Thrnhardt, G. Khitrova, H. M. Gibbs, "Measurement of optical absorption by a single quantum dot exciton", *Physical Review B* **65**, 241310 (2002).

[21] D. Gammon, E. S. Snow, B. V. Shanabrook, D. S. Katzer, D. Park, "Fine Structure Splitting in the Optical Spectra of Single GaAs Quantum Dots", *Physical Review Letters* **76**, 3005 (1996).

[22] M. Bayer, G. Ortner, O. Stern, A. Kuther, A. A. Gorbunov, A. Forchel, P. Hawrylak, S. Fafard, K. Hinzer, T. L. Reinecke, S. N. Walck, J. P. Reithmaier, F. Klopf, F. Schfer, "Fine structure of neutral and charged excitons in self-assembled In(Ga)As/(Al)GaAs quantum dots", *Physical Review B* **65**, 195315 (2002).

[23] D. Gammon, S. W. Brown, E. S. Snow, T. A. Kennedy, D. S. Katzer, D. Park, "Nuclear Spectroscopy in Single Quantum Dots: Nanoscopic Raman Scattering and Nuclear Magnetic Resonance", *Science* **277**, 85 (1997).

[24] C. Becher, A. Kiraz, P. Michler, A. Imamogbrevelu, W. V. Schoenfeld, P. M. Petroff, L. Zhang, E. Hu, "Nonclassical radiation from a single self-assembled InAs quantum dot", *Physical Review B* **63**, 121312 (2001).

[25] V. Zwiller, H. Blom, P. Jonsson, N. Panev, S. Jeppesen, T. Tsegaye, E. Goobar, M. Pistol, L. Samuelson, G. Bjork, "Single quantum dots emit single photons at a time: Antibunching experiments", *Applied Physics Letters* **78**, 2476 (2001).

[26] N. H. Bonadeo, G. Chen, D. Gammon, D. S. Katzer, D. Park, D. G. Steel, "Nonlinear Nano-Optics: Probing One Exciton at a Time", *Physical Review Letters* **81**, 2759 (1998).

[27] N. H. Bonadeo, J. Erland, D. Gammon, D. Park, D. S. Katzer, D. G. Steel, "Coherent Optical Control of the Quantum State of a Single Quantum Dot", *Science* **282**, 1473 (1998).

[28] T. H. Stievater, X. Li, D. G. Steel, D. Gammon, D. S. Katzer, D. Park, C. Piermarocchi, L. J. Sham, "Rabi Oscillations of Excitons in Single Quantum Dots", *Physical Review Letters* **87**, 133603 (2001).

[29] X. Li, Y. Wu, D. G. Steel, D. Gammon, L. J. Sham, "Raman coherence beats from the entangled state involving polarized excitons in single quantum dots", *Physical Review B* **70**, 195330 (2004).

[30] M. V. Gurudev Dutt, J. Cheng, Y. Wu, X. Xu, D. G. Steel, A. S. Bracker, D. Gammon, S. E. Economou, R. Liu, L. J. Sham, "Ultrafast optical control of electron spin coherence in charged GaAs quantum dots", *Physical Review B* **74**, 125306 (2006).

[31] G. Chen, N. H. Bonadeo, D. G. Steel, D. Gammon, D. S. Katzer, D. Park, L. J. Sham, "Optically Induced Entanglement of Excitons in a Single Quantum Dot", *Science* **289**, 1906 (2000).

[32] G. Chen, T. H. Stievater, E. T. Batteh, X. Li, D. G. Steel, D. Gammon, D. S. Katzer, D. Park, L. J. Sham, "Biexciton Quantum Coherence in a Single Quantum Dot", *Physical Review Letters* **88**, 117901 (2002).

[33] X. Li, Y. Wu, D. Steel, D. Gammon, T. H. Stievater, D. S. Katzer, D. Park, C. Piermarocchi, L. J. Sham, "An All-Optical Quantum Gate in a Semiconductor Quantum Dot", *Science* **301**, 809 (2003).

[34] E. D. Kim, K. Truex, X. Xu, B. Sun, D. G. Steel, A. S. Bracker, D. Gammon, L. J. Sham, "Fast Spin Rotations by Optically Controlled Geometric Phases in a Charge-Tunable InAs Quantum Dot", *Physical Review Letters* **104**, 167401 (2010).

CHAPTER 2

Sample Structure, Theoretical Considerations and Experimental Methodology

The sample used in this thesis is an indium arsenide quantum dot grown in a semiconductor heterostructure. The small size of the dot and the highly strained lattice (a cause and consequence of the self assembly process) lead to large changes of the electronic energy structure of the dot compared to the electronic band structure in bulk. This in turn affects the optical characteristics of the dot. In this chapter, we will explore how our sample is fabricated, its optical properties, and the laboratory techniques used in this thesis.

2.1 Sample Structure and Growth

The sample contains InAs self assembled quantum dots (SAQDs) grown by molecular beam epitaxy (MBE) on top of a GaAs Si-doped substrate. First, a 500nm GaAs Te-doped layer is deposited on the substrate to correct for any structural defects in the substrate. The tellurium doping provides donor electrons to charge the quantum dots. This is followed by an 80nm GaAs tunnel barrier. A thin layer of InAs is then deposited on the GaAs. The lattice mismatch between the InAs and GaAs (about 7%) causes the spontaneous formation of InAs droplets (the Stranski-Krastanow growth mode) [1–3] on top of an InAs wetting layer a few monolayers thick (Fig 2.1a inset). An indium flush technique [4,5] is then used to truncate the dots in the vertical direction, controlling their vertical size and shifting the electronic transition energies into a region accessible by the Ti-sapphire lasers used in our laboratory. The dot density
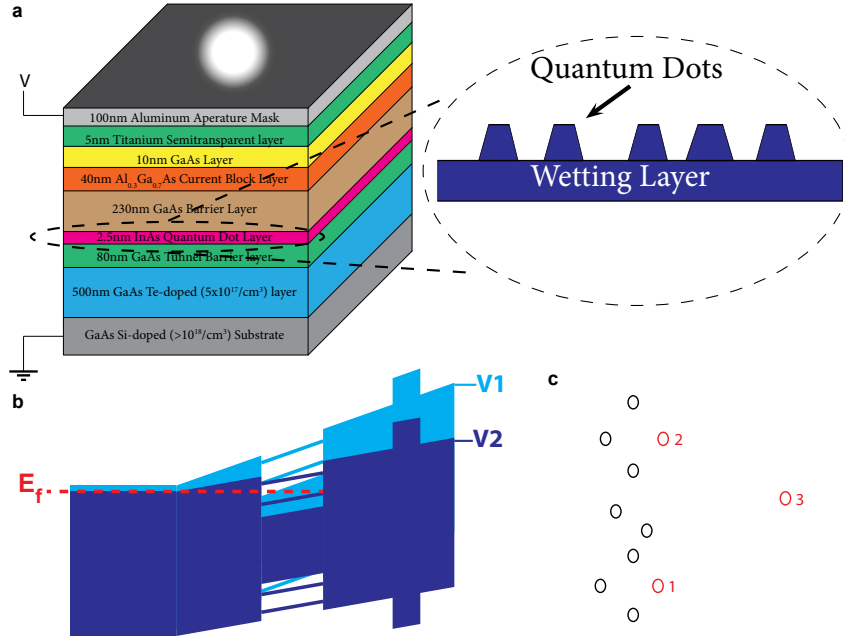
Figure 2.1: (a) Sample structure. The top of the sample is an aluminum aperture mask. (Inset) The self assembled quantum dots form spontaneously on top of the InAs wetting layer after the deposition of about 2 monolayers of InAs. (b) Band bending diagram shows that at voltage V1, the quantum dot energy levels are above the Fermi level, the dot is uncharged. At V2, the quantum dot level is below the Fermi level and thus the dot is charged with a single electron. The left side is the sample bottom while the right side is the top of the sample. (c) A simple diagram of the apertures of interest, labeled 1, 2 and 3. A full aperture map is not available.

is about 1 per square micron. This is followed by the growth of a 230nm GaAs layer, 40nm AlGaAs layer (a current blocking layer), and 10nm GaAs layer. A 5nm semi-transparent layer of Ti is grown on the sample to evenly distribute the electric field when a voltage is applied across the sample[1]. Finally, a 100nm Aluminum aperture mask is deposited (the total sample structure is shown in Fig 2.1a). Micron sized holes etched into the mask via e-beam lithography give us spatial resolution. The presence of the apertures and the low dot density combine with the energy selectivity of continuous wave lasers to give us the ability to selectively excite a single quantum

---

[1]The aperture mask is used as the front contact for applying voltage across the sample. Because there are holes in the mask, field lines will become distorted at the holes, exactly at the location of the accessible quantum dots. The Ti layer is used to redistribute the field lines underneath the aperture mask

dot.

Because the sample is embedded in a Schottky diode structure, we can apply a voltage across the sample to continuously charge the dot with holes and electrons [6–8]. Figure 2.1b shows the spatial dependance of the energy bands. When the sample surface is at voltage V1, the lowest quantum dot energy level in the conduction band is above the Fermi energy (E_f). The dot remains uncharged. When a larger voltage is applied to the sample surface (V2), the bands are bent down so that E_f is now below the Fermi energy, charging the dot with a single electron.

Although it is possible to lithographically pattern the aperture mask, in our sample the apertures are randomly arrayed. This makes it difficult to locate the same aperture (and hence the same quantum dot) if the sample is removed from the cryostat. Furthermore, while the aperture size is ideally $1\mu m$, in reality the aperture size may be larger, probably 2-3μm. While a full aperture map is not available, a local map of the apertures of interest are diagrammed in Fig 2.1c. Aperture 1 contains the exciton used in [9]. Aperture 2 contains the trion used in [10]. Aperture 3 contains the trion used in [11–13].

2.2 Atomic Physics in a Condensed Matter System

From atomic physics, we know that the optical response of an atom is governed by the optical matrix element where the optical selection rules are determined by the symmetry properties of the electron wavefunction [14–17]. In a quantum dot, the electron wavefunction is a Bloch wavefunction. It is a product of a slowly varying envelope which matches the boundary conditions of the quantum dot confining potential, and a quickly varying and periodic "central cell" wavefunction, defined at each atom in the lattice. In this section, we will quickly review condensed matter theory for bulk semiconductors and define the envelope and central cell wavefunctions. This will allow us to derive the surprising result that the optical matrix elements of quantum dot transitions is dominated by the quickly varying central cell wavefunctions, and not by the envelope wavefunctions [1, 18]. Finally, we will review some results in

the literature which calculate the central cell portion of the electron and hole ground state wavefunctions, and find that they are "s" and "p" orbitals, respectively [19].

2.2.1 Bulk Bandstructure and Bloch Wavefunctions

To understand the electronic states in a quantum dot and their interactions with optical fields, we must first consider the electronic states in bulk semiconductors [1,20]. The Schrodinger equation in a simple bulk crystal is given by

$$\hat{H}\Psi = \left\{ \frac{-\hbar}{2m}\nabla^2 + U(r) \right\} \Psi = E\Psi \qquad (2.1)$$

where $U(\vec{r})$ (green in Fig 2.2) is the periodic crystal potential, so that $U(\vec{r}+\vec{R}) = U(\vec{r})$ and $\vec{R}$ is a vector that points to the unit cells (and thus traces over the crystal lattice).
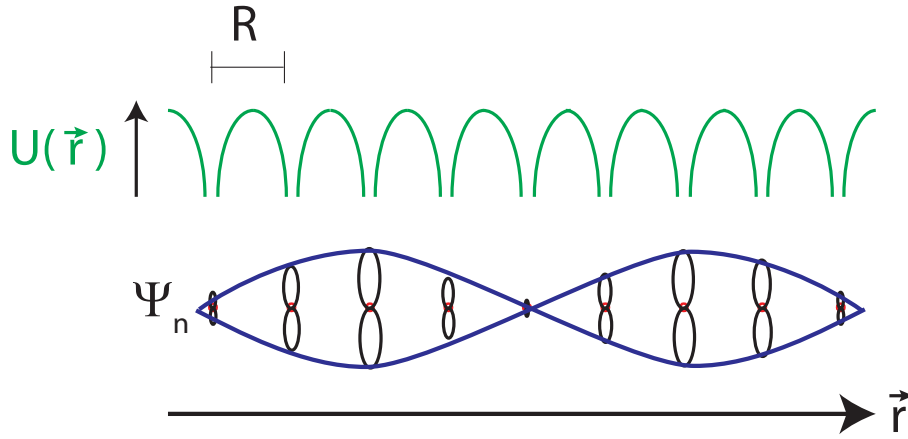
Figure 2.2: For atoms (red dots) in a crystal with periodicity $\vec{R}$, the potential $U(\vec{r})$ (in green) is also periodic with period $\vec{R}$. The electron wavefunction is $\Psi(\vec{r}) = e^{i\vec{k}\cdot\vec{r}}u(\vec{r})$, where the envelope is drawn in blue and the central cell portion is in black.

Bloch's theorem then states that the electronic wave function $\Psi(\vec{r})$ should obey

$$\Psi(\vec{r}) = e^{i\vec{k}\cdot\vec{r}}u(\vec{r}) \qquad (2.2)$$

where $\vec{k}$ is the crystal momentum and $u(\vec{r})$ is a wavefunction which matches the crystal's periodicity, $u(\vec{r}) = u(\vec{r}+\vec{R})$. This is illustrated for a one dimensional crystal

in Fig 2.2, where the envelope function, $e^{i\vec{k}\cdot\vec{r}}$, is drawn in blue and the central cell wavefunction, $u(\vec{r})$, is drawn in black. InAs is a zincblende crystal structure, an FCC lattice with a two atom basis.

In general, the dispersion relation, $E(\vec{k})$, is complicated in crystals. However, in InAs (a direct bandgap material), the dispersion is approximately quadratic at zone center ($\vec{k}=0$). In this case, we can define an *effective mass* for the electron in the crystal like we do for a free electron wave packet

$$\frac{1}{m_{eff}} = \frac{1}{\hbar^2}\frac{d^2E}{dk^2} \tag{2.3}$$

Because the dispersion is not the same as the free space dispersion, the effect mass is very different from the free electron mass. In InAs, $m_{eff} = 0.023m_0$ where m_0 is the free space electron mass. Different effective masses also exist for other $\vec{k}$ values of high symmetry, but our discussion here will be restricted to zone center (aka the Γ point).

The Bloch theorem is a general statement of the form of the wavefunction in periodic potentials. To make further progress, we work in the tight binding approximation where the atomic potential and wavefunctions are used to build up the total crystal Hamiltonian and wavefunctions. We write the total crystal Hamiltonian $\hat{H}_k$ as the sum of the Hamiltonian of each individual atom, $\hat{H}_{atom}$, and $\Delta U(r)$, a perturbation due to the interaction with neighboring atoms.

$$\hat{H}_k = \hat{H}_{\text{atom}} + \Delta U(r) \tag{2.4}$$

Then $\Psi_{\vec{k}}(\vec{r})$ is the total wavefunction satisfying the total Hamiltonian $\hat{H}_k$, with crystal momentum $\vec{k}$, where

$$\hat{H}_k\Psi_k = E_k\Psi_k \tag{2.5}$$

In the tight binding approximation, $\Psi_{\vec{k}}(\vec{r})$ is defined as

$$\Psi_{\vec{k}}(\vec{r}) = \sum_{\vec{R}} e^{i\vec{k}.\vec{R}} \phi(\vec{r} - \vec{R})$$

$$\phi(\vec{r}) = \sum_{n} b_n \psi_n(\vec{r}) \tag{2.6}$$

where ϕ are known as the central cell wavefunctions and are made up of a weighted sum of $\psi_n(\vec{r})$, atomic wavefunctions which satisfy the single atom Hamiltonian ($\hat{H}_{\text{atom}}\psi_n = E_n\psi_n$). The sum over $\vec{R}$ is over all the unit cells of the crystal. Figure 2.2 again illustrates the total wavefunction Ψ_k. The central cell portion ($\phi(\vec{r})$) is drawn in black and is a superposition of atomic wavefunctions ψ_n. Each unit cell (enumerated by $\vec{R}$) has the same ϕ but with a different phase $e^{i\vec{k}.\vec{R}}$ (drawn in blue) determined by the position of the unit cell $\vec{R}$. The total wavefunction is the sum over of the ϕ over all unit cells, each ϕ with its appropriate phase.

The tight binding approximation means that we take the overlap of neighbor atomic wavefunctions to be zero, so that the othogonality relation for atomic wavefunctions becomes

$$\langle \psi_m(\vec{r}) | \psi_n(\vec{r} - \vec{R}) \rangle = \delta_{mn}\delta_{\vec{R}=0} \tag{2.7}$$

the atomic orbits in each unit cell are orthogonal, and wavefunctions of neighboring cells do not overlap.

The electron configuration of In, Ga, and As are:

$$\text{Gallium: } 1s^2 2s^2 p^6 3s^2 p^6 d^1 04s^2 p^1$$

$$\text{Indium: } 1s^2 2s^2 p^6 3s^2 p^6 d^1 04s^2 p^6 d^1 05s^2 p^1 \tag{2.8}$$

$$\text{Arsenic: } 1s^2 2s^2 p^6 3s^2 p^6 d^1 04s^2 p^3$$

Since the outer shell electrons are in the s and p orbitals (orbital angular momentum $l = 0$ and $l = 1$, respectively), we restrict our sum over the atomic wavefunctions ψ_n to these orbitals to make the problem more tractable. The eigenstates and energies are found in the usual way, namely by calculating the various matrix elements of the Hamiltonian

$$\langle\psi_m|H_k|\Psi_k\rangle = E_k\langle\psi_m|\Psi_k\rangle \qquad (2.9)$$

As Ψ_k involves a sum over atomic orbitals, ψ_n this results in various overlap integrals, which can be solved in principle. In practice, however, the tight binding is used as an empirical method, where the overlap integrals are left as fitting parameters and determined through experimental measurement.
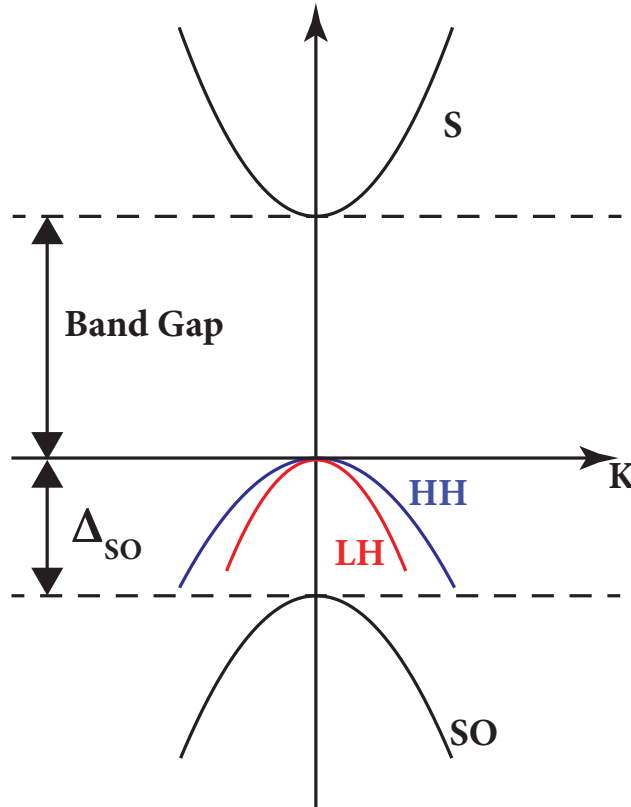
Figure 2.3: This figure shows the conduction and valence band in InAs. The conduction band is labeled "s" and the valence bands are the light hole (LL), heavy hole (HH) and split off (SO) bands.

Detailed calculations of the bandstructure of InAs are beyond the scope of this thesis, but are readily available in the literature [1]. We will simply quote the results here. Figure 2.3 shows the band diagram around zone center ($\vec{k}=0$) for InAs. The band diagram here includes effects of spin orbit coupling where the spin-orbit Hamiltonian is

$$H_{SO} = \lambda \vec{L} \cdot \vec{S} \tag{2.10}$$

where λ is a constant, $\vec{L}$ ($\vec{S}$) is the orbital (spin) angular momentum operator. The conduction band (the lowest energy unoccupied or partially occupied band at zero temperature) is s-like. The orbital angular momentum is zero and the spin angular momentum is $1/2\hbar$. Written in terms of total angular momentum states $|J, m_j\rangle$ (where J=L+S), at zone center ($\vec{k}$=0), the conduction band eigenstate is exactly $\Psi = |1/2, \pm 1/2\rangle$ (in the tight binding approximation).

The effect of spin orbit coupling can be seen in the valence band, which is comprised of p-orbital ($l = 1$) states. The light hole (LH) states ($|3/2, \pm 1/2\rangle$) and heavy hole (HH) states ($|3/2, \pm 3/2\rangle$) are degenerate at zone center and the split off band ($|1/2, \pm 1/2\rangle$) is lower in energy by the spin-orbit splitting, $\Delta \equiv 3\lambda\hbar^2/2$. The "light" and "heavy" hole naming convention derives from the effective mass approximation at zone center. The $|3/2, \pm 3/2\rangle$ band has less curvature and thus has a larger effective mass than the $|3/2, \pm 1/2\rangle$ band. The bandgap of InAs is 0.345eV.

This description of the eigenstates as pure angular moment states (LH, HH, and S) is only valid at zone center. When $k \neq 0$, mixing of the various eigenstates occur. However, from perturbation theory, we know that the amount of state mixing is inversely proportional to the energy difference between the states. We expect that while the LH and HH bands are a mixture of LH and HH states for $k \neq 0$, the conduction and split off bands remain relatively pure. This idea will be important in understanding optical interactions in these materials later.

2.2.2 Optical Properties of Quantum Dots

Although the quantum dot creates a three dimensional confining potential for the electron, we will treat this confining potential as a perturbation on the underlying periodic crystal potential. We still maintain the Bloch form for the electron wavefunction, that is, the wavefunction is the product of an envelope times a central cell wavefunction comprised of atomic orbitals. As we will see by the end of this section,

the allowable transitions and optical selection rules in the quantum dot depend only on the central cell part, and not on the envelope wavefunction.

In a heterostructure, such as a quantum dot, we write the wavefunction in a slightly different form [1, 18, 21].

$$\Psi_{\vec{k}}(\vec{r}) = \sum_n F_n(r)\psi_n(\vec{r}) \tag{2.11}$$

Here, the total wavefunction is the product of some envelope function ($F_n(r)$) times the central cell atomic wavefunctions (ψ_n). The envelope must therefore satisfy the boundary conditions imposed by the heterostructure's confining potential. The envelope is no longer a simple plane wave but some general function. In practice, the envelope can be broken into its Fourier components, and the result is very similar to Eq 2.6. The conceptual difference is that while in bulk, the total Bloch wavefunction has a well defined crystal momentum $\vec{k}$, the eigenstates in the quantum dot are comprised of many such $\vec{k}$'s.

While finding the full energy levels and electron and hole wavefunctions of the quantum dot necessitate a careful calculation using $\vec{k} \cdot \vec{p}$ theory (explained below), there are certain optical properties which do not require this level of detail. We can understand this if we look at the form of the optical interaction. The interaction Hamiltonian between the optical field and the electron [1, 14, 18, 21] is

$$H_{rad} = -\frac{e}{m}\vec{A} \cdot \vec{p} \tag{2.12}$$

where $\vec{A}$ is the field operator and $\vec{p}$ is the electron momentum operator. We have taken the Coulomb gauge and only kept terms linear in $\vec{A}$. The optical interactions are then governed by the optical matrix element $\langle f|H_{rad}|i\rangle$ where $|f\rangle$ ($|i\rangle$) is the final (initial) electronic state. In the dipole approximation, $\vec{A}$ can be moved out of the inner product,

$$H_{fi} = -\frac{e}{m}A\langle f|\hat{e} \cdot \vec{p}|i\rangle \tag{2.13}$$

where $\hat{e}$ is the polarization of the electric field. If we plug in the generic form of the wavefunction in, and realize that $\vec{p} \propto \vec{\nabla}$, we have

$$H_{\text{fi}} \propto \sum_{nm} \langle F_n \psi_n | \hat{e} \cdot \vec{\nabla} | F_m \psi_m \rangle$$

$$= \sum_{nm} \int F_n{}^* \psi_n{}^* \hat{e} \cdot \nabla F_m \psi_m dr \tag{2.14}$$

$$= \sum_{nm} \int F_n{}^* F_m \psi_n{}^* \hat{e} \cdot \nabla \psi_m + F_n{}^* \psi_n{}^* \psi_m \hat{e} \nabla F_m dr \tag{2.15}$$

where the sum over n (m) represents the final (initial) state [1, 18, 21].

Because the envelope functions vary slowly over the unit cell while the central cell wavefunctions vary quick on the order of a unit cell, we can break apart these integrals [1, 18, 21]. The envelope is integrated over the whole structure while the central cell portion is integrated only over a unit cell with volume Ω

$$H_{fi} \propto \sum_{nm} \int F_n{}^* F_m dr \int_\Omega \psi_n{}^* \hat{e} \cdot \nabla \psi_m dr + \int F_n{}^* \hat{e} \cdot \nabla F_m dr \int_\Omega \psi_n{}^* \psi_m dr \tag{2.16}$$

The envelope wavefunction (F) varies over the length scale of the quantum dot while the atom orbital vary on the scale of a unit cell. The gradient term is small for the envelope and the first term in Eq 2.16 is dominant [1, 18, 21]

$$H_{fi} \propto \sum_{nm} \int F_n{}^* F_m dr \int_\Omega \psi_n{}^* \hat{e} \cdot \nabla \psi_m dr \tag{2.17}$$

The integral over Ω can be recognized as the transition dipole moment of a single atom. While the envelope wavefunctions are still general in this treatment and do not have any orthogonality relations, the atomic wavefunctions do. Thus, the allowable transitions and polarization selection rules of those transition are governed by the atomic orbitals which make up the initial and final states and not by the envelope wavefunctions. In Sec 2.2.1, we saw that the eigenfunctions at zone center were atomic s-orbitals in the conduction band and p-orbitals in the valence band. While the construction of the envelope wavefunctions needs to include $\vec{k}$'s for $\vec{k} \neq 0$, if the

dispersion of $\vec{k}$'s remain small and centered at zero, then at least the conduction and valence ground state wavefunctions in the dot will be mostly s-like or p-like, respectively.

2.2.3 Calculating the Wavefunctions in a Quantum Dot using $k \cdot p$ Perturbation Theory

In the above section, we made a handwaving argument about the symmetry of the conduction and valence band wavefunctions. It is entirely possible to calculate the wavefunctions in a more rigorous manner. To lowest order approximation, this problem can be solved by using an effective mass approximation method [22–24]. The electron and hole effective masses are calculated for bulk and the envelope wavefunction and eigenenergies are solved numerically for the confining potential using the effective mass.

However, a more general and accurate method is to use the 8 band $\vec{k}\cdot\vec{p}$ perturbation method [1, 19, 21, 25–28]. $\vec{k} \cdot \vec{p}$ assumes that the eigenenergies and wavefunction are known at some $\vec{k}_0$ and perturbatively solves the bandstructure for $\vec{k} \approx \vec{k}_0$, calculating the amount of band mixing and the eigenstates. For quantum dots, $\vec{k}_0$ is simply $\vec{k}=0$ and the known eigenfunctions are the eight bands found in the tight binding method in Sec 2.2.1 (which are the s and p orbitals at $\vec{k}=0$). The confinement of the electron wavefunction inside the dot necessitate multiple $\vec{k}$'s to construct the envelope wavefunction. The $\vec{k} \cdot \vec{p}$ method is used to calculate the energy of such $\vec{k}$'s and the eigenstates at those $\vec{k}$'s.

In addition to the band offset (that is, the difference between the InAs and GaAs bandgap energies), the quantum dot confining potential also includes strain and strain induced piezoelectric effects which can be accounted for in the $\vec{k} \cdot \vec{p}$ calculations. These effects will introduce additional mixing of bands. Because band mixing is automatically calculated by $\vec{k} \cdot \vec{p}$ theory, this is more accurate than the single band effect mass calculations alluded to above. The details of such calculations are beyond the scope of this work, and can be found in a number of references [1, 19, 21, 25–28].

The results are simply quoted here.
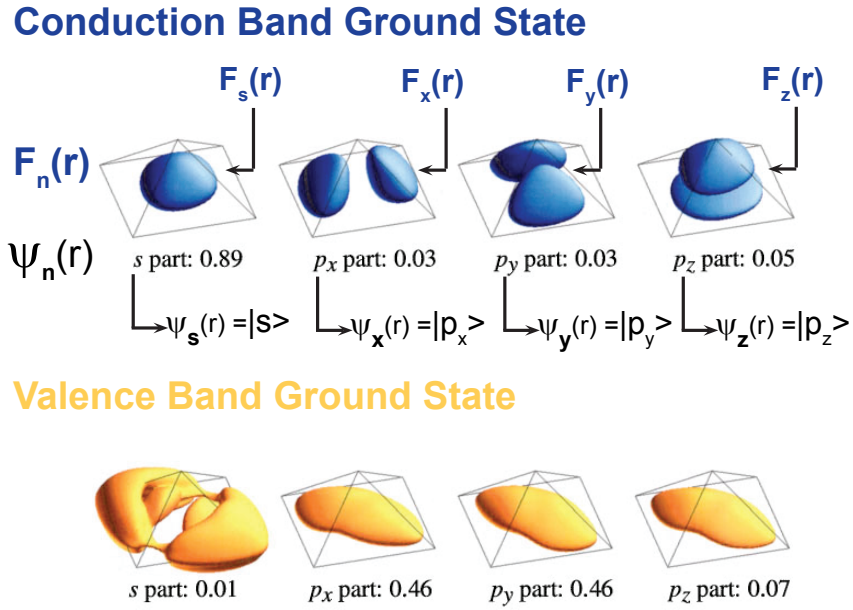
Figure 2.4: The ground state conduction (electron) and valence (hole) wavefunctions are shown. The solid shapes show the envelope wavefunction (F_n) which corresponds to the labeled atomic wavefunction (ψ_n). The numbers give the relative weight (probability) of each component. The total wavefunction is $\Psi_{\vec{k}}(\vec{r}) = \sum_n F_n(r)\psi_n(\vec{r})$. This figure is reprinted with permission from O. Stier, M. Grundmann, and D. Bimberg, Physical Review B, Vol 59, pg 5688 (1998). Copyright (1998) by the American Physical Society.

Recall that Eq 2.11 defined the wavefunction as $\Psi_{\vec{k}}(\vec{r}) = \sum_n F_n(r)\psi_n(\vec{r})$. Figure 2.4 shows calculated wavefunctions reproduced with permission from [19] for the ground state in the conduction (electron) and valence (hole) bands. The colored illustration shows the envelope F_n for a given atomic orbital, ψ_n. For example, the ground conduction wavefunction is $\Psi = 0.89F_s|s\rangle + 0.03F_x|p_x\rangle + 0.03F_y|p_y\rangle + 0.05F_z|p_z\rangle$ where F_s, F_x, F_y and F_z are drawn in blue in Fig 2.4 and $|s\rangle$ and $|p_i\rangle$ are the atomic orbitals. Thus, the ground state conduction wavefunction is primarily an s-orbital whose envelope wavefunction is roughly spherical.

Similarly, the ground state wavefunction in the valence band is the product of an envelope that is elongated along the $[1\overline{1}0]$ direction with a central cell that is comprised almost entirely of heavy hole states. The heavy hole states $|3/2, \pm3/2\rangle$ are

defined as

$$|3/2, 3/2\rangle = \frac{1}{\sqrt{2}}[|p_x\rangle + i|p_y\rangle]|\Uparrow\rangle \qquad (2.18)$$

$$|3/2, -3/2\rangle = \frac{1}{\sqrt{2}}[|p_x\rangle - i|p_y\rangle]|\Downarrow\rangle \qquad (2.19)$$

where $|\Uparrow\rangle$ ($|\Downarrow\rangle$) is the electron spin up(down) state.

In bulk materials, strain lifts the degeneracy of the heavy and light holes at $\vec{k}$=0 [1]. Since self assembled quantum dots are heavily strained, the light hole band is shifted lower in energy. Thus, the top of the valence band is heavy hole in nature and the valence ground state in the quantum dot reflects this. Figure 2.4 shows that the electron and hole envelope wavefunctions are displaced from each other, creating a permanent electric dipole moment for the exciton. This is due to a combination of quantum dot geometry [19] and a gradient of In concentration in the dot along the growth direction [29, 30] (indium rich at the bottom and poor at the top).

In Sec 2.2.2 we found that the transition matrix element for initial and final states in a quantum dot is governed by the atomic transition matrix elements of the central cell wavefunction. We also made a handwaving argument that the central cell portion of the ground states in the conduction and valence bands should remain s like and p like, respectively. In this section, we find that calculations in the literature support our argument, and indeed the conduction band ground state is an s-orbital while the valence band ground state is a heavy hole state (a combination of $|p_x\rangle$ and $|p_y\rangle$ orbitals). These atomic wavefunctions then determine the optical selection rules for low energy transitions in the quantum dot.

When the quantum dot is uncharged, the ground state is the crystal ground state and the optically excited state is the single exciton. There is an anisotropic exchange interaction between the electron and the hole which lifts the degeneracy of the exciton spin states. It also changes the exciton optical selection rules from circular to linear. This results in a three level V-system.

When the dot is charged with a single electron, the ground states are the two electron spin states. The optically excited states are called trion states. The single

electron plus the optically generated exciton create a three quasi-particle system consisting of two electrons and one hole. The two electrons form a spin singlet and so the trion is characterized by its heavy hole. This results in two degenerate two level systems, one with left and the other right - circularly polarized optical transitions.

2.3   Experimental Setup
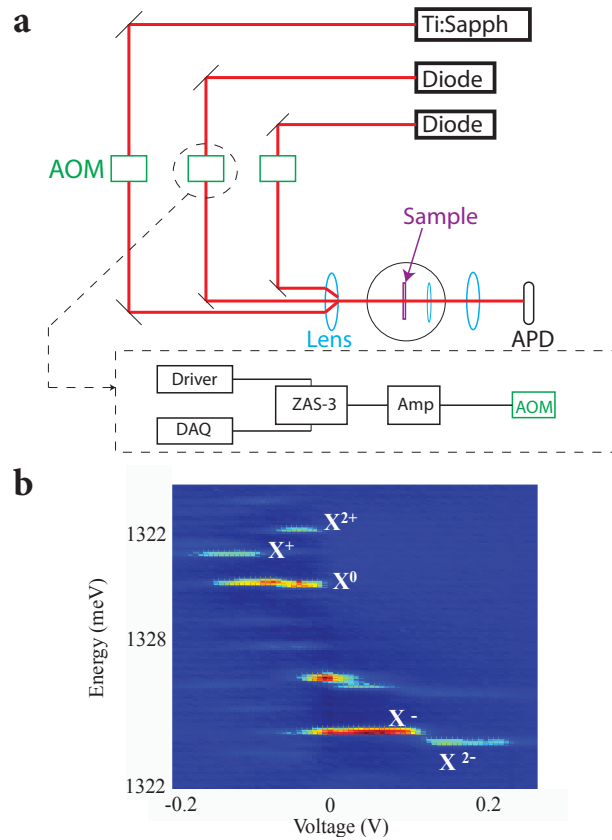
Figure 2.5: (a)The experiments are done using a combination of three continuous wave lasers. One titanium sapphire laser and two diode lasers. These are passed through acousto-optical modulators which can be used to gate the lasers on and off. The sample is held in a helium flow cryostat at 4-5K. (b) Example photoluminescence spectrum showing various charge states of a single quantum dot.

Figure 2.5a shows the laboratory setup used in the experiments that form this thesis. Three continuous wave lasers are used in various combinations throughout this thesis. For earlier experiments, the titanium sapphire laser is an 899-29 ring

laser from Coherent Inc. Later experiments use the MBR 110 titanium sapphire ring laser from Coherent Inc. The two diode lasers are Littman/Metcalf external cavity diode lasers from Sacher Inc. All lasers have a linewidth of less than 1MHz.

For the experiments conducted in Chapters 3 and 4, the lasers are simply focused into the cryostat, bypassing the accousto-optic modulatos (AOMs) seen in 2.5a. The 899-29 is used in Chapters 3 and 4 the 899-29 is used while in Chapter 5 the 899 is replaced by a MBR 110 and all three lasers are passed through traveling wave(AOMs in Fig 2.5a). The inset of Fig 2.5a shows how the AOMs are controlled to gate the lasers. A 40MHz driving signal is created by a signal generator and switched via a MiniCircuits ZAS-3 attenuator/switch, controlled by an analog voltage from the National Instruments DAQ (data acquisition) board. The resulting signal is amplified by an RF amplifier and used to drive the AOMs. When the DAQ voltage is 1V, the AOM is "on" and the laser beam is deflected into the first order diffraction mode of the AOM, which is the focused onto the sample. When the DAQ voltage is 0V, the AOM is "off" and no first order beam is present. DAQ voltages between 0-1V can be used to attenuate the power in the first order diffracted beam.

The sample is held in a helium flow magneto cryostat from Janis Research Company Inc. at a temperature of 4-5K. The lasers are focused onto the sample and propagate along the sample growth axis ($\vec{z}$ axis). An external magnetic field can be applied perpendicular to the optical axis ($\vec{x}$ axis), known as the Voigt geometry. This splits and mixes the trion spin states, creating a four level system where the spin flip Raman transitions are turned on. This will be discussed in detail in Chapter 3. The lasers pass through the sample and are focused on a silicon avalanche photodiode (APD in Fig 2.5a). For photoluminescence (PL) experiments, the light is instead focused into a spectrometer. A DC bias applied across the sample controllably charges the quantum dot. Figure 2.5b shows the various charge states of the quantum dot in PL.

When an AC component is added to the bias, the absorption resonances are periodically shifted according to the DC modulation frequency (usually 1-4KHz). The transmission signal on the APD is fed into a lock in amplifier which is a phase sensi-

tive method to suppress the background laser noise and measure the laser absorption signal. This is known as Stark shift modulation spectroscopy [31]. When the AC magnitude is small, the measured signal is the derivative of the true absorption line-shape. In this thesis, we use a large DC modulation voltage to directly measure the lineshape without the need to integrate.

2.4 Summary In this chapter, we first explored the details of the quantum dot sample structure and growth technique. The sample is comprised of InAs self as-sembled quantum dots grown in a Schottky diode structure which allows controllable charging of the dots. Next, we reviewed some basic condensed matter theory and found that the optical properties of the dot are governed by the atomic orbitals of the individual atoms. A review of the literature shows that the ground state electron wavefunction has a central cell portion that is an s-orbital while the ground state hole wavefunction is a heavy hole. Finally, we detailed the experimental setup used in this thesis.

BIBLIOGRAPHY

BIBLIOGRAPHY

[1] J. Singh, *Physics of Semiconductors and Their Heterostructures*, McGraw-Hill Education (ISE Editions), ISBN 0071128352 (1993).

[2] P. M. Petroff, A. Lorke, A. Imamoglu, "Epitaxially Self-Assembled Quantum Dots", *Physics Today* **54**, 46 (2001).

[3] A. J. Ramsay, "A review of the coherent optical control of the exciton and spin states of semiconductor quantum dots", *Semiconductor Science and Technology* **25**, 103001 (2010).

[4] T. H. Stievater, X. Li, D. G. Steel, D. Gammon, D. S. Katzer, D. Park, C. Piermarocchi, L. J. Sham, "Rabi Oscillations of Excitons in Single Quantum Dots", *Physical Review Letters* **87**, 133603 (2001).

[5] J. R. Guest, T. H. Stievater, X. Li, J. Cheng, D. G. Steel, D. Gammon, D. S. Katzer, D. Park, C. Ell, A. Thränhardt, G. Khitrova, H. M. Gibbs, "Measurement of optical absorption by a single quantum dot exciton", *Physical Review B* **65**, 241310 (2002).

[6] A. Zrenner, L. V. Butov, M. Hagn, G. Abstreiter, G. Böhm, G. Weimann, "Quantum dots formed by interface fluctuations in AlAs/GaAs coupled quantum well structures", *Physical Review Letters* **72**, 3382 (1994).

[7] D. Gammon, E. S. Snow, B. V. Shanabrook, D. S. Katzer, D. Park, "Fine Structure Splitting in the Optical Spectra of Single GaAs Quantum Dots", *Physical Review Letters* **76**, 3005 (1996).

[8] H. Drexler, D. Leonard, W. Hansen, J. P. Kotthaus, P. M. Petroff, "Spectroscopy of Quantum Levels in Charge-Tunable InGaAs Quantum Dots", *Physical Review Letters* **73**, 2252 (1994).

[9] X. Xu, B. Sun, P. R. Berman, D. G. Steel, A. S. Bracker, D. Gammon, L. J. Sham, "Coherent Optical Spectroscopy of a Strongly Driven Quantum Dot", *Science* **317**, 929 (2007).

[10] X. Xu, Y. Wu, B. Sun, Q. Huang, J. Cheng, D. G. Steel, A. S. Bracker, D. Gammon, C. Emary, L. J. Sham, "Fast Spin State Initialization in a Singly Charged InAs-GaAs Quantum Dot by Optical Cooling", *Physical Review Letters* **99**, 097401 (2007).

[11] X. Xu, B. Sun, E. D. Kim, K. Smirl, P. R. Berman, D. G. Steel, A. S. Bracker, D. Gammon, L. J. Sham, "Single Charged Quantum Dot in a Strong Optical

Field: Absorption, Gain, and the ac-Stark Effect", *Physical Review Letters* **101**, 227401 (2008).

[12] X. Xu, B. Sun, P. R. Berman, D. G. Steel, A. S. Bracker, D. Gammon, L. J. Sham, "Coherent population trapping of an electron spin in a single negatively charged quantum dot", *Nat Phys* **4**, 692 (2008).

[13] X. Xu, W. Yao, B. Sun, D. G. Steel, A. S. Bracker, D. Gammon, L. J. Sham, "Optically controlled locking of the nuclear field via coherent dark-state spectroscopy", *Nature* **459**, 1105 (2009).

[14] P. R. Berman, V. S. Malinovsky, *Principles of Laser Spectroscopy and Quantum Optics*, Princeton University Press, ISBN 0691140561 (2010).

[15] C. Cohen-Tannoudji, J. Dupont-Roc, G. Grynberg, *Atom-Photon Interactions: Basic Processes and Applications* (1998).

[16] P. Meystre, M. Sargent, *Elements of Quantum Optics*, Springer, 4th edition, ISBN 3540742093 (2007).

[17] M. O. Scully, M. S. Zubairy, *Quantum Optics*, Cambridge University Press, 1 edition, ISBN 0521435951 (1997).

[18] S. L. Chuang, *Physics of Optoelectronic Devices*, Wiley-Interscience, ISBN 0471109398 (1995).

[19] O. Stier, M. Grundmann, D. Bimberg, "Electronic and optical properties of strained quantum dots modeled by 8-band k·p theory", *Physical Review B* **59**, 5688 (1999).

[20] N. W. Ashcroft, N. D. Mermin, *Solid State Physics*, Brooks Cole, 001 edition, ISBN 0030839939 (1976).

[21] D. Gershoni, C. Henry, G. Baraff, "Calculating the optical properties of multidimensional heterostructures: Application to the modeling of quaternary quantum well lasers", *Quantum Electronics, IEEE Journal of* **29**, 2433 (1993).

[22] M. A. Cusack, P. R. Briddon, M. Jaros, "Electronic structure of InAs/GaAs self-assembled quantum dots", *Physical Review B* **54**, R2300 (1996).

[23] M. A. Cusack, P. R. Briddon, M. Jaros, "Absorption spectra and optical transitions in InAs/GaAs self-assembled quantum dots", *Physical Review B* **56**, 4047 (1997).

[24] J. Marzin, G. Bastard, "Calculation of the energy levels in quantum dots", *Solid State Communications* **92**, 437 (1994).

[25] H. Jiang, J. Singh, "Conduction band spectra in self-assembled InAs/GaAs dots: A comparison of effective mass and an eight-band approach", *Applied Physics Letters* **71**, 3239 (1997).

[26] H. Jiang, J. Singh, "Strain distribution and electronic spectra of InAs/GaAs self-assembled dots: An eight-band study", *Physical Review B* **56**, 4696 (1997).

[27] H. Jiang, J. Singh, "Radiative and non-radiative inter-subband transition in self assembled quantum dots", *Physica E: Low-dimensional Systems and Nanostructures* **2**, 720 (1998).

[28] H. Jiang, J. Singh, "Strain tensor and electron and hole spectra in self-assembled InGaAs/GaAs and SiGe/Si quantum dots", *Physica E: Low-dimensional Systems and Nanostructures* **2**, 614 (1998).

[29] P. W. Fry, I. E. Itskevich, D. J. Mowbray, M. S. Skolnick, J. J. Finley, J. A. Barker, E. P. O'Reilly, L. R. Wilson, I. A. Larkin, P. A. Maksym, M. Hopkinson, M. Al-Khafaji, J. P. R. David, A. G. Cullis, G. Hill, J. C. Clark, "Inverted Electron-Hole Alignment in InAs-GaAs Self-Assembled Quantum Dots", *Physical Review Letters* **84**, 733 (2000).

[30] J. J. Finley, M. Sabathil, P. Vogl, G. Abstreiter, R. Oulton, A. I. Tartakovskii, D. J. Mowbray, M. S. Skolnick, S. L. Liew, A. G. Cullis, M. Hopkinson, "Quantum-confined Stark shifts of charged exciton complexes in quantum dots", *Physical Review B* **70**, 201308 (2004).

[31] B. Alen, F. Bickel, K. Karrai, R. J. Warburton, P. M. Petroff, "Stark-shift modulation absorption spectroscopy of single quantum dots", *Applied Physics Letters* **83**, 2235 (2003).

CHAPTER 3

Three Level Systems, Lambda and V

As we saw in Chapter 2, neutral quantum dots can be considered to be three level systems while singly charged dots are four level systems under applied magnetic field in the Voigt geometry. This Chapter will explore the different types of nonlinear optical physics that can be realized in the three level V system of a neutral dot and the three level lambda (Λ) subsystem of a singly charged dot. Because the quantum dot is by its nature a complex many-body problem [1], strong optical excitation in the V system should allow us to probe any deviations from the theoretical model we developed in Chapter 2. An ideal V system should exhibit both Autler-Townes and Mollow absorption spectra under intense optical excitation. However, the neutral exciton is not the ideal system for quantum computation and information processing. If the qubit states involve the excited states, then the excited state decay will necessarily introduce qubit dephasing. Instead, we charge the quantum dot with a single electron and use the electron spin as our qubit. A magnetic field in the Voigt geometry creates a four level optically accessible system where the two lambda (Λ) subsystems are useful energy subsystems to manipulate the electron spin qubit. Here, optical pumping can be used to quickly initialize the spin and coherent population trapping and dark state physics can be used to generate and measure electron spin coherence.

3.1 V System [2]

31
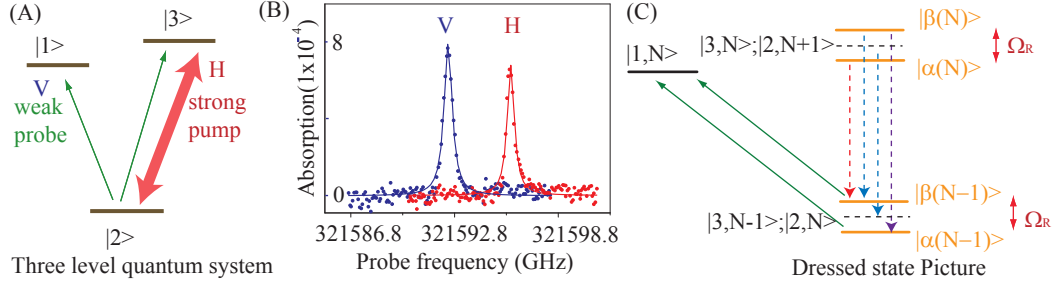
Figure 3.1: (a) The neutral quantum dot three level V system. Strong excitation effects in the probe (green arrows) absorption spectrum can be seen when a strong pump (red arrow) is resonant with transition H. (b) Single beam absorption spectrum of the neutral quantum dot, showing two orthogonal transitions split by the anisotropic exchange splitting. The solid lines are fits to Lorentzians. (c) Dashed lines show the quantized atom field states with no interaction. When the atom-field interaction is turned on, the degeneracy is lifted, resulting in the solid lines.

As we alluded to in Chapter 2, the energy level structure of a neutral quantum dot is a three level V system whose excited states are the anisotropic exchange [3] split exciton states, shown in Fig 3.1a. These excited states ($|1\rangle$ and $|3\rangle$) are optically coupled to the crystal ground state ($|2\rangle$) via linearly polarized transitions, V and H respectively. When a probe scans across the transitions, they show up simply as Lorentizian peaks in the probe absorption spectrum. To study the V-system, we locate a neutral exciton in aperture 1 (see Sec 2.1). The photoluminescence spectrum and characterization of the DC Stark shift for this state is available in [4]. The absorption spectrum for the exciton is seen in Fig 3.1b where the solid lines are fits to Lorenztians. The linearly polarized light only excites the corresponding linearly polarized transition, with virtually no coupling to the orthogonal transition. In this case, the exchange splitting is about 15μeV or about 3.6GHz and the linewidth of the transition is about 1.8μeV, or about 440MHz.

When a strong pump is placed on transition H (Fig 3.1a), the probe absorption spectrum is significantly modified. When the probe scans across the V transition, it sees an Autler-Townes split doublet [5], while transition H will show the Mollow absorption spectrum [6–10]. In the following experiments, the pump and probe lasers

are 45° cross polarized, so that the pump beam can be blocked before the detector. The strong field excitation regime is defined by $\Omega_{pump} >> 2\gamma$, where $\Omega_{pump} \equiv \frac{\mu E_{pump}}{\hbar}$ is the pump Rabi frequency, γ is the transition dephasing rate, μ is the transition dipole moment, and E_{pump} is the amplitude of the electric field of the pump laser.

3.1.1   Autler-Townes Splitting

Figure 3.1c shows the fully quantized atom-field states, the Jaynes-Cummings ladder, where the field mode are resonant with their respective transitions. The Jaynes-Cummings Hamiltonian [11] for a single mode optical field is

$$H = \hbar\frac{\omega_0}{2}\sigma_z + \hbar\omega a^\dagger a + \hbar g \left(\sigma_+ a + a^\dagger\sigma_-\right) \tag{3.1}$$
$$g = -i(\frac{\omega}{2\hbar\epsilon_0\nu})^{1/2}\mu$$

where ω_0 is the transition frequency, ω is the laser frequency, σ are the Pauli matrices, a are the field raising and lowering operators and "g" is the vacuum Rabi frequency. The first term is the atomic Hamiltonian and the second term is the field Hamiltonian, while the last term is the atom-field interaction Hamiltonian. When the field is resonant with transition H ($\omega = \omega_0$) and the interaction is off, the "bare" ground states $|3, N-1\rangle$ and $|2, N\rangle$ are degenerate (dashed lines), where N labels the photon number of the driving field. When the atom-field interaction is turned on, the degeneracy is lifted, the states are mixed, producing "dressed" states [11, 12] $|\alpha, N-1\rangle$ and $|\beta, N-1\rangle$ separated by energy $\hbar\Omega_{pump}$, shown as the solid lines.

When a weak probe scan across transition V, the probe absorption spectrum is split into two peaks, known as Autler-Townes splitting. The probe effectively sees absorption from two ground states, $|\alpha, N-1\rangle$ and $|\beta, N-1\rangle$, separated by Ω_{pump}. This is seen experimentally in Fig 3.2a, where the probe absorption is plotted for various pump intensities. The data are shifted vertically for clarity. There is a small energy shift of the response relative to the low intensity excitation that is probably due to a small screening of the applied field by photoexcited charge in the diode.
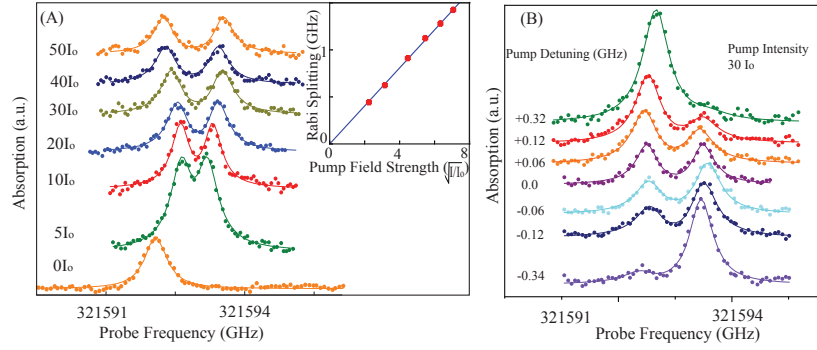
Figure 3.2: Autler-Townes absorption spectra for (a) resonant pump and various pump intensities and (b) fixed pump intensity and various pump detunings. Inset (a) shows the splitting of the Autler-Townes sidebands as a function of pump field strength. Solid lines are fits. $I_0 = 1.2W/cm^2$

The shift saturates at a power between the lowest intensity curve and the next higher power spectrum. The pump laser is adjusted to follow the shift of the resonance.

Clearly, the once Lorentzian probe absorption profile is spilt into two Aulter-Townes peaks by the pump. We plot the measured splitting as a function of the square root of the pump intensity in the inset of Fig 3.2a. It depends linearly on the pump field strength and goes to zero in the absence of the pump, as expected for the dependence of the Autler-Townes splitting on the Rabi frequency. Figure 3.2b shows the probe absorption as a function of the pump detuning with a fixed pump intensity of $30I_0$ (the corresponding photon number per unit volume is approximately $1.4 \times 10^{10}/cm^3$), where $I_0 = 1.2W/cm^2$, corresponding to a Rabi frequency of approximately $\Omega/2\pi = 1.1GHz$. Again, the data are shifted for clarity.

To fit our data, we model the system in the semiclassical approximation(in contrast to the Jaynes-Cummings model above), where the quantum dot electronic states are treated quantum mechanically and the optical field is treated classically [11]. We solve the density matrix equations for a three level system for first order in the probe and all orders of the pump. The equation of motion of the density matrix $\rho_{ij} \equiv \sum_{ij} |i\rangle\langle j|$ is

$$i\frac{d\rho}{dt} = [H, \rho] + Decay \tag{3.2}$$

where H is the Hamiltonian and *Decay* is a matrix representing the population and coherence decay terms.

To zeroth order of the probe and all orders of the pump, the system simply behaves as a two level system, with

$$\overset{0}{\rho}_{22} = 1 - \frac{\gamma \Omega_d^2}{2\left(\Gamma \delta_d^2 + \gamma\left(\gamma\Gamma + \Omega_d^2\right)\right)}$$
$$\overset{0}{\rho}_{23} = \frac{i\Gamma\left(\gamma + i\delta_d\right)\Omega_d}{2\left(\Gamma \delta_d^2 + \gamma\left(\gamma\Gamma + \Omega_d^2\right)\right)} \tag{3.3}$$

where Ω_d is the pump Rabi frequency, Γ is the excited state decay rate, γ is the transition dephasing rate, and δ_d is the pump detuning.

Solving for first order in the probe, we find that the probe absorption, proportional to ρ_{12} in the Maxwell-Bloch approach [11], is

$$\alpha = -\alpha_0 Im\left[\frac{2i\left(2\left(\delta - i\gamma_{31} - \delta_d\right)\overset{0}{\rho}_{22} + \Omega_p\overset{0}{\rho}_{23}\right)}{4(\gamma + i\delta)\left(\delta - i\gamma_{31} - \delta_d\right) - i\Omega_p^2}\right] \tag{3.4}$$

where α_0 is a constant, δ is the probe detuning, and γ_{31} is the dephasing rate of the $|3\rangle$ to $|1\rangle$ transition. In the absence of pure dephasing, γ_{31} should be half the decay rate of $|1\rangle$ plus half the decay rate of $|3\rangle$, so $\gamma_{31} = \Gamma$. Detailed calculations are given in Appendix A. It's easy to see that for $\Omega_d > \gamma, \gamma_{31}$, Eq 3.4 produces two resonances centered at $\delta = -\frac{1}{2}\left(\delta_d \pm \sqrt{\delta_d^2 + \Omega_d^2}\right)$. The fits are shown as the solid lines in Fig 3.2.

Autler-Townes splitting can provide a means to measure the optical dipole moment, as the Rabi frequency is a product of the transition dipole moment with the optical field. From the extracted Rabi splitting with the corresponding optical field strength, we can infer a transition dipole moment of about 30 Debye for this particular QD. The Einstein A coefficient (spontaneous emission rate) of a QD in a medium [13] is given as $\gamma_{\text{sp}} = \frac{9n^2}{\left(2n^2 + n_{\text{QD}}^2\right)^2}\frac{\omega_0^3\mu^2}{3\pi\epsilon_0\hbar c^3} = \frac{9n^2}{\left(2n^2 + n_{\text{QD}}^2\right)^2}\gamma_{\text{sp0}}$, where n (n_{QD}) is the refractive index of the medium (quantum dot), and γ_{sp0} is the spontaneous emission rate of a two-level quantum system in the vacuum. By taking $n = n_{QD}$, inserting the experimental parameters and the extracted dipole moment into the equation, we obtain

$\gamma_{sp}/2\pi = 190MHz$, which corresponds to a life time of about 840 ps. Assuming there is no other decay and no pure dephasing, this would lead to a natural linewidth expected in the low power absorption spectrum also equal to $\gamma/2\pi = 190MHz$. Compared to the extracted line width from the single beam, low power absorption data, which is about 500 MHz, γ_{sp} is about 2.5 times smaller. This discrepancy indicates that there is possibly a spectral wandering process [14] or non-radiative relaxation process which broadens the transition linewidth. Previous studies have shown that there is an absence of pure dephasing in these quantum dot systems [4].

3.1.2 Mollow Absorption Spectrum
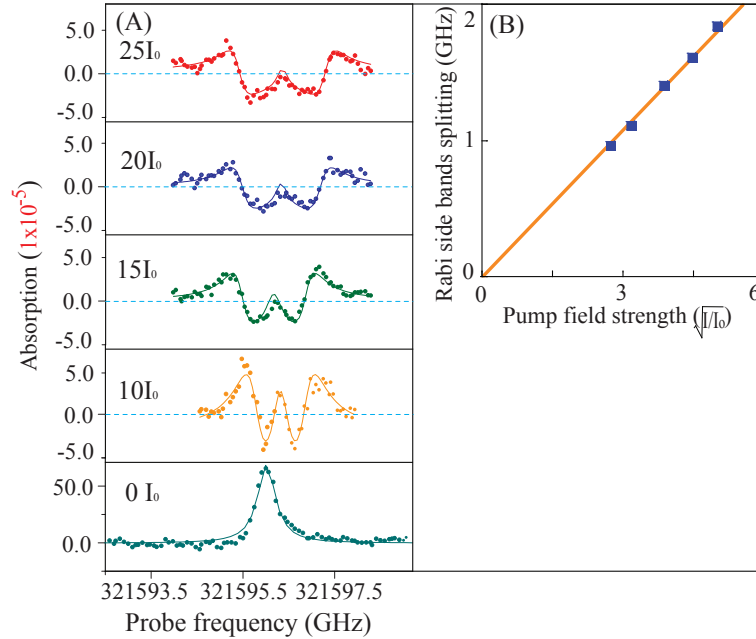
Figure 3.3: (a) The Mollow absorption spectrum for various pump intensities. The dashed line represents zero absorption. The solid lines are fits.(b) Splitting of the Rabi sidebands as a function of the pump field strength. $I_0 = 1.2W/cm^2$

From Fig 3.1c, and the previous discussion of dressed states, one would expect that under strong resonant excitation, the fluorescence spectrum of the H transition would show three peaks. One peak would be centered at resonance, corresponding to the two degenerate transitions indicated by the blue dashed lines, and two at $\pm\Omega_R$,

indicated by the red and purple dashed lines. Indeed, this is known as the Mollow triplet [6–10, 15]. However, the absorption spectrum of a weak probe coupled to the H transition is not so easily understood in the dressed state picture. Figure 3.3a shows the absorption spectrum of the weak probe for various pump intensities. The resulting lineshape is a W, where we observe a relatively weak maximum centered at zero probe detuning and two Rabi side bands with dispersive lineshapes. The spectral shift of the data with the high power field is due to the excitation of charge states in the buffer layer. The complex lineshape of the MAS depends strongly on the pump intensity. The splitting between the two side bands is plotted as a function of the square root of the pump intensity in Fig. 3.3b, again showing that the splitting linearly depends on the pump field strength and is zero in the absence of the pump field.

The data shows that the probe beam experiences optical gain in the pump-probe configuration for strong excitation. The data in Fig. 3.3a show that part of the probe absorption curve is below zero, indicating gain. Using the data corresponding to 15Io as an example, the absorption/gain ratio is about $0.066\%/0.0024\% = 27.5$. This gain is from the pump and probe beams coherently exchanging energy through the QD and corresponds to gain without inversion since there is no population inversion either in the dressed or bare atom pictures.

To understand the lineshape, we again solve the density matrix equations for the system in the semiclassical approximation. Once again, we consider the pump to all orders and the probe to first order. We find that the absorption profile is given by:

$$\alpha = \alpha_0 Im[\frac{2i\gamma\Gamma(\gamma + i\delta)(\Gamma + i\delta) + \Gamma\delta\Omega_d^2}{2(\gamma + i\delta)\left(\gamma\Gamma + \Omega_d^2\right)\left((\gamma + i\delta)(\Gamma + i\delta) + \Omega_d^2\right)}] \tag{3.5}$$

Detailed calculations are given in Appendix B. At $\delta \approx \Omega_d$, this can be rewritten as

$$\alpha_{\rm ms} = \pm\alpha_0\frac{\Gamma}{\Omega_d}\frac{(\delta \mp \Omega_d)}{4\left(\delta \mp \Omega_d\right)^2 + (\Gamma + \gamma)^2} \tag{3.6}$$

Equation 3.6 shows that the absorption profile is the sum of two dispersive lineshapes with zero crossings at $\delta = \pm\Omega$. For $|\delta| < \Omega_d$, the absorption is negative, that

is, the probe sees gain. However, at exactly $\delta = 0$, the gain is canceled by a small absorptive component. The data is fit using equation 3.5, shown as the solid lines in Fig 3.3.

3.1.3 Summary

The results of our experiments in the strong excitation regime are in good agreement with theoretical predictions of both Autler-Townes splitting and the Mollow absorption spectrum. This demonstrates that the quantum dot behaves as an isolated quantum system, whose discrete energy levels are maintained at high optical field strengths. Furthermore, the quantum dot can be used as an optical modulator [16] where a pump beam optically modulates the transmission of a probe beam through the Mollow absorption spectrum.

3.2 Λ System

We set the bias voltage across the sample to charge the dots with a single electron and locate a suitable charged exciton transition in photoluminescent in Aperture 3 (see Chapter 2). The single negatively charge exciton, called the trion, is about 5.5meV lower in energy than the neutral exciton state. The trion is a three particle system formed by a spin singlet pair and one hole. The projection of the hole angular momentum on the sample growth direction determines the angular momentum of the trion state to be $|\pm\frac{3}{2}\rangle$. At zero magnetic field, the electron spin ground states $|\pm\frac{1}{2}\rangle$ are two fold degenerate. The only dipole allowed transition is from the spin up $|\frac{1}{2}\rangle$ (spin down $|-\frac{1}{2}\rangle$) state to the trion $|\frac{3}{2}\rangle$ ($|-\frac{3}{2}\rangle$) state with σ^+ (σ^-) excitation. Since the spin flip transitions are not allowed here, there is no way to optically coherently control our electron spin qubit.

Figure 3.4 shows the trion four level model with a magnetic field applied in the Voigt geometry along the $\vec{X}$ axis (perpendicular to the sample growth and optical axis, $\vec{z}$), where $|x\pm\rangle$ ($|t\pm\rangle$)are the spin (hole) eigenstates under the magnetic field. This mixes and splits the spin states of both the electron ground state and the hole
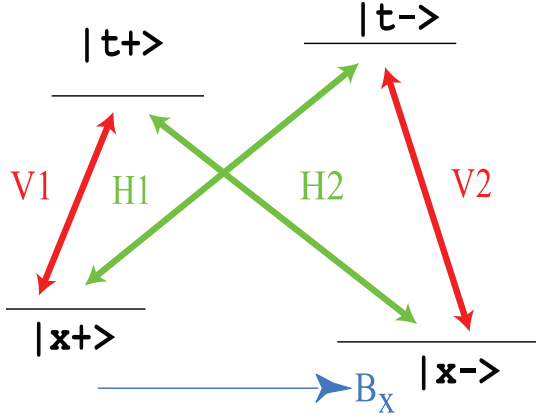
Figure 3.4: Trion four level energy diagram under applied magnetic field in the Voigt geometry ($\vec{B}\|\vec{x} \perp$ growth direction). This mixes and splits the spin states, lifting the degeneracy, turning on all four optical transitions.

excited state, turning on the spin flip Raman transitions. We now have an energy level structure which will allow us to optically manipulate our electron spin qubit.

The Zeeman splitting of the electron spin (trion) states is $|g_{e\perp}\mu_B B_x|(|g_{h\perp}\mu_B B_x|$), where$g_{e\perp}$ ($g_{h\perp}$) is the electron (hole) spin in-plane gfactor, μ_B is Bohr magneton, and B_x is the applied magnetic field. The four transitions are labeled as V1, H1, H2, and V2.

When a single laser beam is resonant with any of the transitions, population is optically pumped from one ground state to the other. This allows fast spin initialization and spin cooling [17,18]. If two lasers are set so that they couple the two different ground states to the same excited state, a lambda (Λ) three level energy subsystem is formed. Here, the coherence of the lasers can be imparted to the electron spin [19,20], allowing the initialization of the electron to an arbitrary coherent superposition state. In this section, we will investigate these two effects.

3.2.1 Optical Pumping [18]

Figure 3.5a shows the voltage modulation [21] absorption map [22] as a function of the applied voltage bias at a magnetic field of 0.88 T. The laser field is linearly
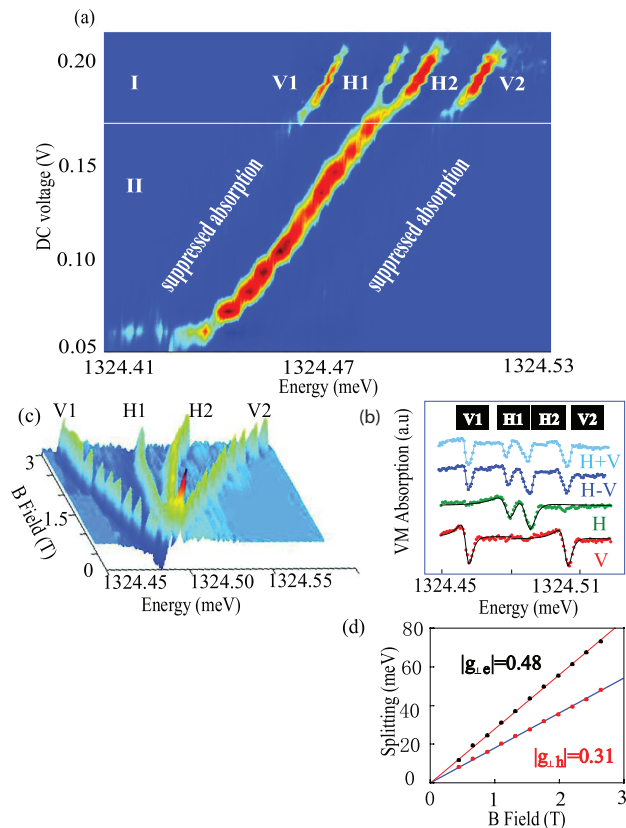
Figure 3.5: (a)Single laser absorption map as a function of probe laser energy and applied DC voltage. (b) Probe absorption spectrum for various probe polarizations. (c)Probe absorption map as a function of probe energy and applied magnetic field. Voltage is set so the electron is in the co-tunneling region. (d)Electron and hole Zeeman splittings are plotted as a function of applied magnetic field. The fits give the electron and hole g factors.

polarized and 45^0 to the polarization axis of the QD. Fast spin cooling is demonstrated in bias region II, where the absorption of the laser beam is strongly suppressed, as marked in Fig 3.5(a).

In region II of Fig 3.5a, spin relaxation is suppressed. When the laser beam is on resonance with transition V1, the electron spin in $|x+\rangle$ spin state will be excited to the trion state $|t+\rangle$ and then relax back to the two spin ground states with comparable relaxation rates as suggested by the comparable absorption strengths and linewidths. That is to say, because the spin flip resonant Raman scattering process is now allowed in the Voigt profile, the optical induced spin flip process is dramatically sped up,

ensuring a fast spin cooling. Since the electron spin in the ground state has a much slower relaxation rate than the trion spontaneous decay rate, the electron spin will be optically pumped into the $|x-\rangle$ spin state within a few radiative cycles. Since the $|x+\rangle$ state is depleted and the spin population is trapped in the $|x-\rangle$ state, the signature of optical pumping is that transition V1 becomes transparent to the laser beam. The preparation of $|x+\rangle$ works in a similar way. This is clearly demonstrated in the voltage range II of Fig 3.5a. When the laser is on resonance with V1(V2), the absorption is strongly suppressed and the transition becomes transparent. Thus, the polarized spin states can be selectively prepared in either the $|x+\rangle$ or $|x-\rangle$ spin state.

The quartet transition pattern appears in bias region I, where the optical pumping effect fades away. The is because the voltage is set so that the electron is no longer stably trapped in the dot. Here, co-tunneling induced (the tunneling of the electron between the quantum dot and Fermi sea) spin flip [17,23] causes fast spin relaxation, repopulating the depleted ground state.

The data in the transition region from I to II in Fig. 3.5a show the signature of a bias dependent electron g factor, which leads to transitions H1 and H2 evolving from two well-resolved lines in region I into a central absorption peak in region II. Since transitions H1 and H2 are nearly degenerate in region II, when the laser is on resonance with transition H1, it is also nearly resonant with H2. Therefore, the optical pumping effect is partially canceled by the bidirectional pumping induced by the same optical field. Hence, the optical pumping effect is suppressed and results in the central absorption peak. The origin of this behavior remains under investigation, but it is likely that the strong bias dependence is more complex than the bias dependent g factors reported earlier in quantum wells [24] and for hole in QDs [25]. Fortunately, the behavior does not impact the main qualitative conclusion of the work.

Figure 3.5b shows the polarization study of the trion state at gate voltage 0.19 V. A quartet transitions pattern is excited with a 45^0 linearly polarized light. When the light is vertically (horizontally) polarized, the optical field only excites the outer (inner) two transitions of the quartet. Thus, the inner and outer transitions are strictly linearly polarized and orthogonal to each other, which inhibits spontaneously

generated coherence (SGC) [26].

Our measurements confirm that the dark transitions become bright and all the transitions are linearly polarized. However, the polarization axis $(\vec{\rho})$ is not parallel or perpendicular to the applied magnetic field direction, instead it is 45° to $\vec{B}$. This observation indicates the existence of heavy and light hole mixing in our dots, which is due to the QD in-plane anisotropy. Our observation agrees with the previous reports on CdSe/ZnSe SAQDs [27], and the mixing effects have been discussed in detail in Ref [4].

Setting the gate voltage to be in the co-tunneling region, we gradually ramp the magnetic field and map the probe absorption as a function of the field (Fig 3.5c). By plotting the splitting of the electron and hole spin states as a function of the external field, (Fig 3.5d), we can fit the splittings and extract an electron and hole g factors of 0.48 and 0.31, respectively. Although our method only gives the magnitude of the g-factors, we know that they must have the same sign.
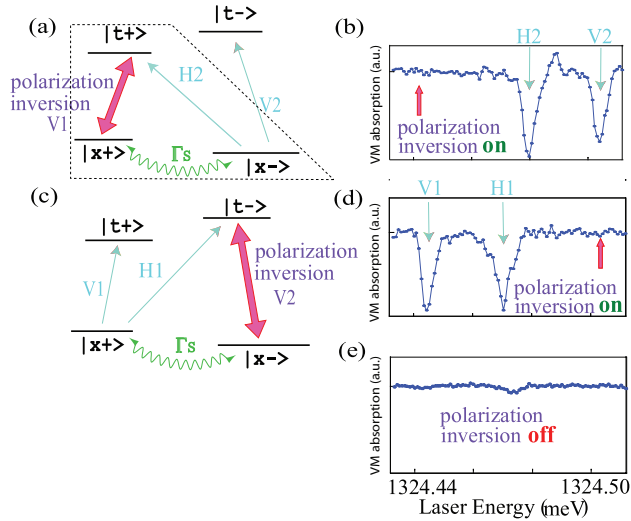
Figure 3.6: (a)Placing an additional laser, a polarization inversion beam, on transition V1 recovers absorption on transitions H2 and V2, seen in (b). (c)Placing a polarization inversion beam on transition V2 recovers absorption transition V1 and H1, seen in (d). (e)Without the polarization inversion beam, optical pumping renders all transitions transparent. The magnetic field has been increased to 1.32T, lifting the degeneracy of the H1 and H2 transitions.

In order to prove that the laser beam prepares the spin state as $|x-\rangle$ ($|x+\rangle$) by pumping the V1 (V2) transition, a strong optical field (polarization inversion beam) is tuned to be on resonance with the transition V2 (V1) while increasing the magnetic field to 1.32T to lift the H1 H2 degeneracy. As shown in Fig. 3.6b, while the polarization inversion beam is tuned to be on resonance with the transition V1, it depolarizes the polarized spin state ($|x+\rangle$) created by the beam pumping the transition V2 (i.e. redistribute the population between the spin ground states). This leads to the recovery of the absorption of the transitions V2 and H2. Figures 3.6c and d shows that the transitions V1 and H1 can also be recovered by tuning the polarization inversion beam to be on resonance with the transition V2. Considering that spin cooling prepares a low-entropy polarized spin state, the effect of the polarization inversion beam is to increase the entropy of the system by generating mixed spin ground states. For comparison, Fig. 3.6e shows the absorption spectrum without the polarization inversion beam at magnetic field 1.32 T and gate voltage 0.12 V. As expected, all transitions become transparent.

From our data and theory [28] we find that the optical pumping rate is about $0.4 \times \Gamma_{t+x-} = 3.8 \times 10^9 s^{-1}$. Furthermore, at a magnetic field of 0.88T, we experimentally achieve a spin state preparation efficiency of 98.9%, which, assuming a Maxwell-Boltzmann distribution, corresponds to a spin temperature of 0.06 K [17, 29]. This is somewhat limited by off-resonant coupling. Because the trion energy level structure is ultimately a four level system, optical pumping on one leg of a Λ subsystem will off resonantly couple to the same polarization leg of the second Λ subsystem, causing a small repumping to occur [28]. This limits the pumping efficiency, although higher magnetic fields can reduce this effect. Detailed calculations of the optical pumping rate can be found in Ref [4, 18, 28]

3.2.2 Coherent Population Trapping and Dark State Physics [30]

Unlike the neutral exciton, the four level system of the trion and optical pumping effects prevent us from studying V system physics in the trion system. Instead, if we
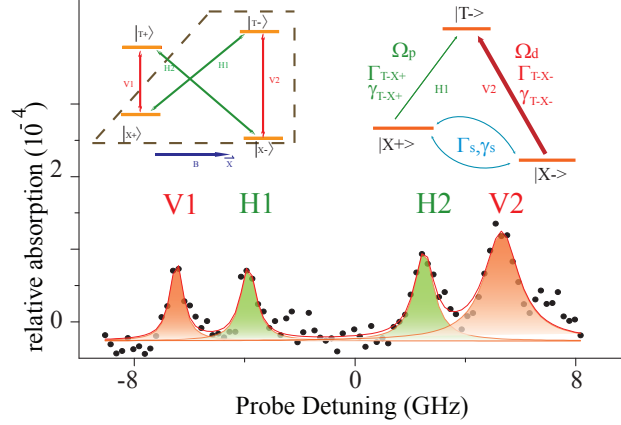
Figure 3.7: We choose the lambda subsystem shown in the dashed outline by selectively exciting transitions H1 and V2 with narrow linewidth continuous wave lasers. The system is modeled using the constants shown, where Ω is the Rabi frequency, γ is a coherence dephasing rate, and Γ is a population decay rate.

selectively excite transitions H1 and V2, we can select out the Λ subsystem shown in Fig 3.7. To understand the physics present here, we will first consider the system in the amplitude picture without any decay [11], with $|x+\rangle=|1\rangle$, $|x-\rangle=|3\rangle$, $|t-\rangle=|2\rangle$, Ω_d (Ω_p) the pump (probe) Rabi frequency, ω_d (ω_p) the pump (probe) laser frequency, and $\hbar\omega_i$ the energy of state $|i\rangle$. The time dependent state vector can be defined as $|\Psi\rangle=a_1|1\rangle + a_2|2\rangle + a_3|3\rangle$. In this case, the amplitudes of the states, a_i, evolve as:

$$i\dot{a}_2 = \chi_p e^{-i\omega_p t} a_1 \ + \chi_d e^{-i\omega_d t} a_3 \tag{3.7}$$

$$i\dot{a}_1 = -\omega_1 a_1 \ + \chi_p e^{i\omega_p t} a_2 \tag{3.8}$$

$$i\dot{a}_3 = -\omega_3 a_3 \ + \chi_d e^{i\omega_d t} a_2 \tag{3.9}$$

where $\chi \equiv \frac{\Omega}{2}$. In the field interaction picture, we take $a_1 = c_1 e^{i\omega_p t}; a_3 = c_3 e^{i\omega_d t}; a_2 = c_2$ and define probe and pump detunings $\delta_p = \omega_p - \omega_1$ and $\delta_d = \omega_d - \omega_1$ the equations become

$$i\dot{c}_1 = \delta_p c_1 + \chi_p c_2 \tag{3.10}$$

$$i\dot{c}_2 = \chi_p c_1 + \chi_d c_3 \tag{3.11}$$

$$i\dot{c}_3 = \delta_d c_3 + \chi_d c_2 \tag{3.12}$$

In the field interaction picture, $|1\rangle$ has energy $\hbar\delta_p$ and $|3\rangle$ has energy $\hbar\delta_d$. Multiplying Eq 3.10 by χ_d and Eq 3.12 by χ_p, these equations can be transformed to:

$$i\left(\chi_d \dot{c}_1 - \chi_p \dot{c}_3\right) = \chi_d \delta_p c_1 - \chi_p \delta_d c_3 \tag{3.13}$$

$$i\dot{c}_2 = \chi_p c_1 + \chi_d c_3 \tag{3.14}$$

$$i\left(\chi_d \dot{c}_1 + \chi_p \dot{c}_3\right) = \chi_d \delta_p c_1 + \chi_p \delta_d c_3 + 2\chi_d \chi_p c_2 \tag{3.15}$$

It is trivial to see that at the two photon resonance, $\delta_p = \delta_d \equiv \delta$, we can create new basis states $|B\rangle = \frac{\chi_d |1\rangle + \chi_p |3\rangle}{\sqrt{\chi_d{}^2 + \chi_p{}^2}}$ and $|D\rangle = \frac{\chi_d |1\rangle - \chi_p |3\rangle}{\sqrt{\chi_d{}^2 + \chi_p{}^2}}$. Now, we rewrite the amplitude equations in the new basis

$$i\dot{c}_D = \delta c_D \tag{3.16}$$

$$i\dot{c}_2 = \sqrt{\chi_d{}^2 + \chi_p{}^2} c_B \tag{3.17}$$

$$i\dot{c}_B = \delta c_B + 2\frac{\chi_d \chi_p}{\sqrt{\chi_d{}^2 + \chi_p{}^2}} c_2 \tag{3.18}$$

On the two photon resonance, the two optical fields act coherently as a single field in the interaction picture, coupling only the $|B\rangle$ state, the bright state, to the excited state $|2\rangle$. This behavior is much like the optical pumping behavior we studied previously. The population will be pumped into $|D\rangle$, the dark state, where it is trapped. The system will then become transparent to the laser fields. This way, we can initialize the system into a coherent superposition state. The coherence, defined as ρ_{x+x-}, is equal to $\frac{\chi_d \chi_p}{\chi_d{}^2 + \chi_p{}^2}$ in the absence of any decay. Furthermore, by simply changing the ratio of pump to probe Rabi frequencies, it is possible to initialize the system into any arbitrary superposition of spin ground states.

Ultimately, if we set Ω_d to zero, the initialized spin state will be $|x+\rangle$. This is simply due to the optical pumping effect discussed previously. The difference is that when Ω_d is zero, there is no coherence involved in the state initialization, and the preparation efficiency is determined by the electron spin relaxation rate. In the initialization of the coherent superposition state, we generate an electron spin coherence by the optical fields, so the state preparation efficiency is limited by the electron spin decoherence rate [11].

In the presence of decay and dephasing, we can solve the optical Bloch equations as we have done previously [11], using the various decay constants given in Fig 3.7 where Γ are population decay rates and γ are dephasing rates. At the two photon resonance, we find the probe absorption to be

$$\alpha = \alpha_0 \frac{(\gamma_s - \Gamma_s + \lambda^2 \Gamma_s)}{(1 + \lambda^2)^2} \frac{\gamma_{T-X+}}{\Omega_d^2} \tag{3.19}$$

where $\lambda = \Omega_p / \Omega_d$. In the limit of no spin relaxation or dephasing ($\gamma_s = \Gamma_s = 0$), the absorption is identically zero, as predicted by our amplitude picture calculation.

In our experiment, a strong optical field (the driving field) is tuned on resonance with transition V2 and a weak optical field (the probe) is scanned across transition H1. When the probe laser is resonant with transition H1, the two-photon Raman resonance condition is reached. As seen in Fig. 3.8b, a clear dip in the probe absorption spectrum is observed for $\Omega_d = 0.56$GHz. This observation demonstrates both the coherent population trapping of an electron spin and the generation of Raman coherence between the spin ground states. As the absorption does not identically go to zero in at the two photon resonance, we know that the spin dephasing rate is non-zero. When the pump is off, optical pumping renders the H1 transition transparent to the probe, and no absorption is seen (Fig 3.8a). The applied magnetic field is 2.64T, corresponding to an electron Zeeman splitting of 18.2GHz.

The linewidth of the dip in the probe absorption spectrum is ultimately limited by the electron spin decoherence rate. In the experiment, the smallest Ω_d we applied is 0.56GHz, which is about half of the trion transition linewidth, but still much larger than γ_s. Hence, the linewidth of the dip is broadened by the laser power. When Ω_d is
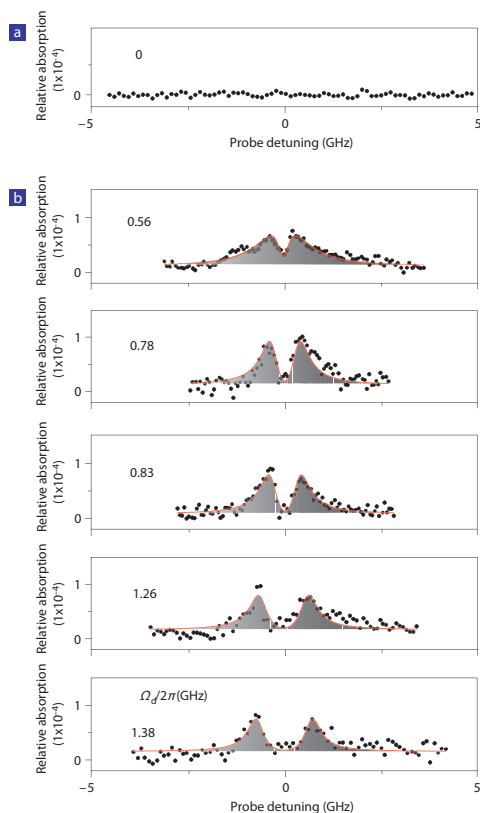
Figure 3.8: (a)When the pump is off, the probe absorption is zero due to optical pumping. (b)Probe absorption spectrum for various pump intensities. The central dip is the dark state dip.

strong, it will dress the spin ground state $|x-\rangle$ and the trion state $|t-\rangle$. In the case where Ω_d is larger than the trion transition linewidth, $|t-\rangle$ is Rabi split, and the probe absorption exhibits Autler-Townes splitting as described in the previous section. The spectral features of the probe absorption spectrum in our experiment is a combination of the Autler-Townes splitting and the coherent population trapping (CPT) quantum interference effect, where the spectral positions of the side bands can be determined by the Autler-Townes splitting and the central feature in the absorption spectrum is due to the CPT effect, not a simple summation of the tails of the Autler-Townes Lorentzian lineshapes.

The probe absorption spectra with various driving field and fixed probe Rabi frequencies are illustrated in Fig. 3.8b. The energy separation of the two peaks increases with the pump field intensity. As Ω_d becomes larger than the trion transition

linewidth, two Autler-Townes peaks with Lorentzian lineshapes appear in the probe absorption spectrum. Figure 3.9a plots the splitting of the Rabi sidebands as a function of the driving field strength. A linear regression fits the data and extends to zero in the absence of the driving field, which indicates that the splitting is dominated by Ω_d. The red solid lines on top of the data shown in Fig. 3.8b are the theoretical fits obtained by solving the optical Bloch equations to all orders in the driving field and to first order in the probe. Assuming that γ_s is a few orders of magnitude larger than Γ_s, we find $\gamma_{t-x+}/2\pi = 0.54 \pm 0.1 MHz$ and $\gamma_s = 40 \pm 12 MHz$. The spin coherence time $T2* \equiv 1/\gamma_s$ is about 4ns. Although we measure an electron spin trapped inside a single QD, the electron spin extracted from the data is not the intrinsic electron spin decoherence time due to the hyperfine interaction [31–34] between the electron spin and the neighboring nuclei ensemble. The intrinsic T2 can be measured by spin echo [35] or mode locking of spin coherence techniques [36].

The generation of the dark state is accompanied by the creation of electron spin coherence, which corresponds to the density matrix element ρ_{x+x-} . By inserting the parameters extracted from the fits into the optical Bloch equations and calculate values for the spin coherence, which are represented by the red line in Fig. 3.9(b). The green line in Fig. 3.9(b) represents the theoretical values for the coherence in the absence of spin decoherence, given by $\frac{\chi_d \chi_p}{\sqrt{\chi_d{}^2 + \chi_p{}^2}}$. The blue line represents the ratio of the experimentally generated coherence to the ideal case. The light blue dash vertical lines indicate the applied Ω_d in the experiment. At the maximally applied Rabi frequency 1.38 GHz, we infer that 94% of the optimal coherence is generated in our system.

3.3 Summary

In this Chapter, we have shown that the physics of three level systems feature prominently in quantum dots. In neutral dots, the anisotropic splitting of the optically generated exciton creates a three level system. We probe the strong excitation regime of the neutral dot and see both Autler-Townes splitting and the Mollow absorption

spectrum. This signifies that the dot behaves as a well isolated quantum system even under intense optical excitation. Additionally, the presence of gain without inversion in the Mollow excitation geometry can form the basis of an optically controlled optical modulator.

For a singly charged dot, applying a magnetic field perpendicular to the growth direction lifts the ground and excited state spin degeneracies and mixes the spin states, creating a four level system. The three level subsystems can then be used to optically manipulate the electron spin states. A single beam can quickly initialize the spin into a spin up, or spin down state, while two lasers can initialize the electron into an arbitrary superposition state via coherent population trapping.

Interestingly, in the absence of decay, the V and λ systems are mathematically identical. How is it then that they behave so differently under optical excitation? Aulter-Townes splitting can be shown to be equivalent to the summation of two Lorenztians, centered at $\pm\Omega_{pump}$. The Lorenztian tails overlap in the central dip, and absorption there never reaches zero. In the Λ system, however, the probe absorption at the two photon resonance can be identically zero in the absence of spin dephasing. The answer lies partly in the physics of the decay processes. In the V system, the dephasing between the excited state, γ_{31} is limited by the excited state decay rate, Γ. In the Λ system, coherent population trapping is inherently an optical pumping process whose pumping *rate* depends on the excited state decay. However, the pump *efficiency* is ultimately governed by the coherent dark state and ground state spin dephasing rate, a value that is physically independent of excited state decay processes and can be an arbitrary value.

BIBLIOGRAPHY

BIBLIOGRAPHY

[1] L. J. Sham, T. M. Rice, "Many-Particle Derivation of the Effective-Mass Equation for the Wannier Exciton", *Physical Review* **144**, 708 (1966).

[2] X. Xu, B. Sun, P. R. Berman, D. G. Steel, A. S. Bracker, D. Gammon, L. J. Sham, "Coherent Optical Spectroscopy of a Strongly Driven Quantum Dot", *Science* **317**, 929 (2007).

[3] D. Gammon, E. S. Snow, B. V. Shanabrook, D. S. Katzer, D. Park, "Fine Structure Splitting in the Optical Spectra of Single GaAs Quantum Dots", *Physical Review Letters* **76**, 3005 (1996).

[4] X. Xu, *Coherent Optical Spectroscopy of a Single Semiconductor Quantum Dot.*, Ph.D. thesis, University of Michigan, Ph.D. (2008).

[5] S. H. Autler, C. H. Townes, "Stark Effect in Rapidly Varying Fields", *Physical Review* **100**, 703 (1955).

[6] E. Baklanov, V. Chebotaev, *Sov. Phys. JETP* **34**, 490 (1972).

[7] B. R. Mollow, "Stimulated Emission and Absorption near Resonance for Driven Systems", *Physical Review A* **5**, 2217 (1972).

[8] S. Haroche, F. Hartmann, "Theory of Saturated-Absorption Line Shapes", *Physical Review A* **6**, 1280 (1972).

[9] F. Y. Wu, S. Ezekiel, M. Ducloy, B. R. Mollow, "Observation of Amplification in a Strongly Driven Two-Level Atomic System at Optical Frequencies", *Physical Review Letters* **38**, 1077 (1977).

[10] M. T. Gruneisen, R. W. Boyd, K. R. MacDonald, "Induced gain and modified absorption of a weak probe beam in a strongly driven sodium vapor", *Journal of the Optical Society of America B* **5**, 123 (1988).

[11] P. R. Berman, V. S. Malinovsky, *Principles of Laser Spectroscopy and Quantum Optics*, Princeton University Press, ISBN 0691140561 (2010).

[12] C. Cohen-Tannoudji, J. Dupont-Roc, G. Grynberg, *Atom-Photon Interactions: Basic Processes and Applications* (1998).

[13] A. Thrnhardt, C. Ell, G. Khitrova, H. M. Gibbs, "Relation between dipole moment and radiative lifetime in interface fluctuation quantum dots", *Physical Review B* **65**, 035327 (2002).

[14] A. Hogele, S. Seidl, M. Kroner, K. Karrai, R. J. Warburton, B. D. Gerardot, P. M. Petroff, "Voltage-Controlled Optics of a Quantum Dot", *Physical Review Letters* **93**, 217401 (2004).

[15] B. R. Mollow, "Power Spectrum of Light Scattered by Two-Level Systems", *Physical Review* **188**, 1969 (1969).

[16] S. G. Carter, V. Birkedal, C. S. Wang, L. A. Coldren, A. V. Maslov, D. S. Citrin, M. S. Sherwin, "Quantum Coherence in an Optical Modulator", *Science* **310**, 651 (2005).

[17] M. Atature, J. Dreiser, A. Badolato, A. Hogele, K. Karrai, A. Imamoglu, "Quantum-Dot Spin-State Preparation with Near-Unity Fidelity", *Science* **312**, 551 (2006).

[18] X. Xu, Y. Wu, B. Sun, Q. Huang, J. Cheng, D. G. Steel, A. S. Bracker, D. Gammon, C. Emary, L. J. Sham, "Fast Spin State Initialization in a Singly Charged InAs-GaAs Quantum Dot by Optical Cooling", *Physical Review Letters* **99**, 097401 (2007).

[19] H. R. Gray, R. M. Whitley, J. Stroud, "Coherent trapping of atomic populations", *Optics Letters* **3**, 218 (1978).

[20] S. E. Harris, "Electromagnetically Induced Transparency", *Physics Today* **50**, 36 (1997).

[21] B. Alen, F. Bickel, K. Karrai, R. J. Warburton, P. M. Petroff, "Stark-shift modulation absorption spectroscopy of single quantum dots", *Applied Physics Letters* **83**, 2235 (2003).

[22] S. Seidl, M. Kroner, P. A. Dalgarno, A. Hgele, J. M. Smith, M. Ediger, B. D. Gerardot, J. M. Garcia, P. M. Petroff, K. Karrai, R. J. Warburton, "Absorption and photoluminescence spectroscopy on a single self-assembled charge-tunable quantum dot", *Physical Review B* **72**, 195339 (2005).

[23] J. M. Smith, P. A. Dalgarno, R. J. Warburton, A. O. Govorov, K. Karrai, B. D. Gerardot, P. M. Petroff, "Voltage Control of the Spin Dynamics of an Exciton in a Semiconductor Quantum Dot", *Physical Review Letters* **94**, 197402 (2005).

[24] G. Salis, Y. Kato, K. Ensslin, D. C. Driscoll, A. C. Gossard, D. D. Awschalom, "Electrical control of spin coherence in semiconductor nanostructures", *Nature* **414**, 619 (2001).

[25] M. F. Doty, M. Scheibner, I. V. Ponomarev, E. A. Stinaff, A. S. Bracker, V. L. Korenev, T. L. Reinecke, D. Gammon, "Electrically Tunable g Factors in Quantum Dot Molecular Spin States", *Physical Review Letters* **97**, 197202 (2006).

[26] M. V. G. Dutt, J. Cheng, B. Li, X. Xu, X. Li, P. R. Berman, D. G. Steel, A. S. Bracker, D. Gammon, S. E. Economou, R. Liu, L. J. Sham, "Stimulated and Spontaneous Optical Generation of Electron Spin Coherence in Charged GaAs Quantum Dots", *Physical Review Letters* **94**, 227403 (2005).

[27] A. V. Koudinov, I. A. Akimov, Y. G. Kusrayev, F. Henneberger, "Optical and magnetic anisotropies of the hole states in Stranski-Krastanov quantum dots", *Physical Review B* **70**, 241305 (2004).

[28] C. Emary, X. Xu, D. G. Steel, S. Saikin, L. J. Sham, "Fast Initialization of the Spin State of an Electron in a Quantum Dot in the Voigt Configuration", *Physical Review Letters* **98**, 047401 (2007).

[29] A. Hogele, M. Kroner, S. Seidl, K. Karrai, M. Atature, J. Dreiser, A. Imamoglu, R. J. Warburton, A. Badolato, B. D. Gerardot, P. M. Petroff, "Spin-selective optical absorption of singly charged excitons in a quantum dot", *Applied Physics Letters* **86**, 221905 (2005).

[30] X. Xu, B. Sun, P. R. Berman, D. G. Steel, A. S. Bracker, D. Gammon, L. J. Sham, "Coherent population trapping of an electron spin in a single negatively charged quantum dot", *Nat Phys* **4**, 692 (2008).

[31] A. V. Khaetskii, D. Loss, L. Glazman, "Electron Spin Decoherence in Quantum Dots due to Interaction with Nuclei", *Physical Review Letters* **88**, 186802 (2002).

[32] W. A. Coish, D. Loss, "Hyperfine interaction in a quantum dot: Non-Markovian electron spin dynamics", *Physical Review B* **70**, 195340 (2004).

[33] A. C. Johnson, J. R. Petta, J. M. Taylor, A. Yacoby, M. D. Lukin, C. M. Marcus, M. P. Hanson, A. C. Gossard, "Triplet-singlet spin relaxation via nuclei in a double quantum dot", *Nature* **435**, 925 (2005).

[34] A. S. Bracker, E. A. Stinaff, D. Gammon, M. E. Ware, J. G. Tischler, A. Shabaev, A. L. Efros, D. Park, D. Gershoni, V. L. Korenev, I. A. Merkulov, "Optical Pumping of the Electronic and Nuclear Spin of Single Charge-Tunable Quantum Dots", *Physical Review Letters* **94**, 047402 (2005).

[35] J. R. Petta, A. C. Johnson, J. M. Taylor, E. A. Laird, A. Yacoby, M. D. Lukin, C. M. Marcus, M. P. Hanson, A. C. Gossard, "Coherent Manipulation of Coupled Electron Spins in Semiconductor Quantum Dots", *Science* **309**, 2180 (2005).

[36] A. Greilich, D. R. Yakovlev, A. Shabaev, A. L. Efros, I. A. Yugova, R. Oulton, V. Stavarache, D. Reuter, A. Wieck, M. Bayer, "Mode Locking of Electron Spin Coherences in Singly Charged Quantum Dots", *Science* **313**, 341 (2006).
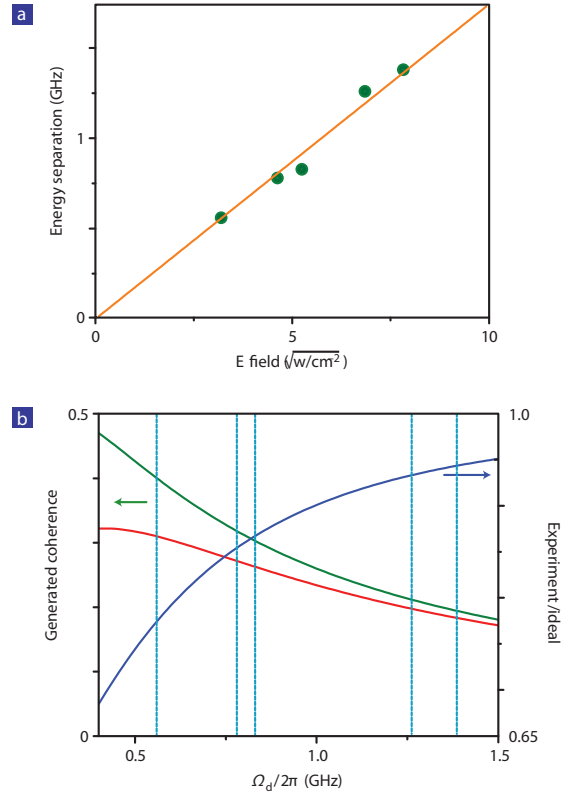
Figure 3.9: (a)Plot of the splitting of the Autler-Townes sidebands as a function of pump field strength. (b)Theoretical curves of the creation of the electron spin coherence in a single charged quantum dot. Red line: experimentally generated electron spin coherence inferred from the optical Bloch equations calculation by using the experimental parameters. The calculation is done under the experimental condition that the driving and probe fields are resonant with transition V2 and H1, respectively. Green line: the calculated maximum electron spin Raman coherence in the absence of the electron spin dephasing. Blue line: the ratio of the calculated coherence with and without electron spin dephasing.

CHAPTER 4

Optically Locking the Nuclear Magnetic Field via Coherent Dark State Spectroscopy

In Chapter 2, we laid out a conceptual understanding of the electronic states and their optical properties in quantum dots based on perturbations about the bulk electronic states. We found that the optical properties of the quantum dot can be approximated by the atomic transitions of the constituent atoms. In Chapter 3, we performed experiments which showed that the atomic theory used to solve simple, stationary three- and four-level systems could accurately model the optical transitions in a quantum dot. However, we know that the reality is more complicated. The quantum dot contains $10^4 - 10^5$ nuclear spins which interact with the electron [1–3]. The nuclear spins create an average magnetic field known as the Overhauser field [1], whose fluctuations is significant cause of electron spin dephasing. The electron spin also produces an effective magnetic field, known as the Knight field [4], which than can be used to control the nuclear spins. The focus of this chapter will be a discussion about a different hyperfine interaction, one between the *hole* spin and the nuclei. This interaction is capable of dynamically polarizing the nuclear spin ensemble and contains an intrinsic feedback mechanism that can be used to control both the average value of the Overhauser field as well as suppress the fluctuations which broaden the width of the Overhauser field distribution. First, we will look at some experimental data which will motivate our theoretical discussion of the hole-nuclear hyperfine interaction. Properly motivated, we will discuss the theory of the electron and hole hyperfine interaction. We will then see some experimental data

which reflects the theoretical predictions.

4.1 Experimental Evidence for Hole Assisted Dynamic Nuclear Spin Polarization
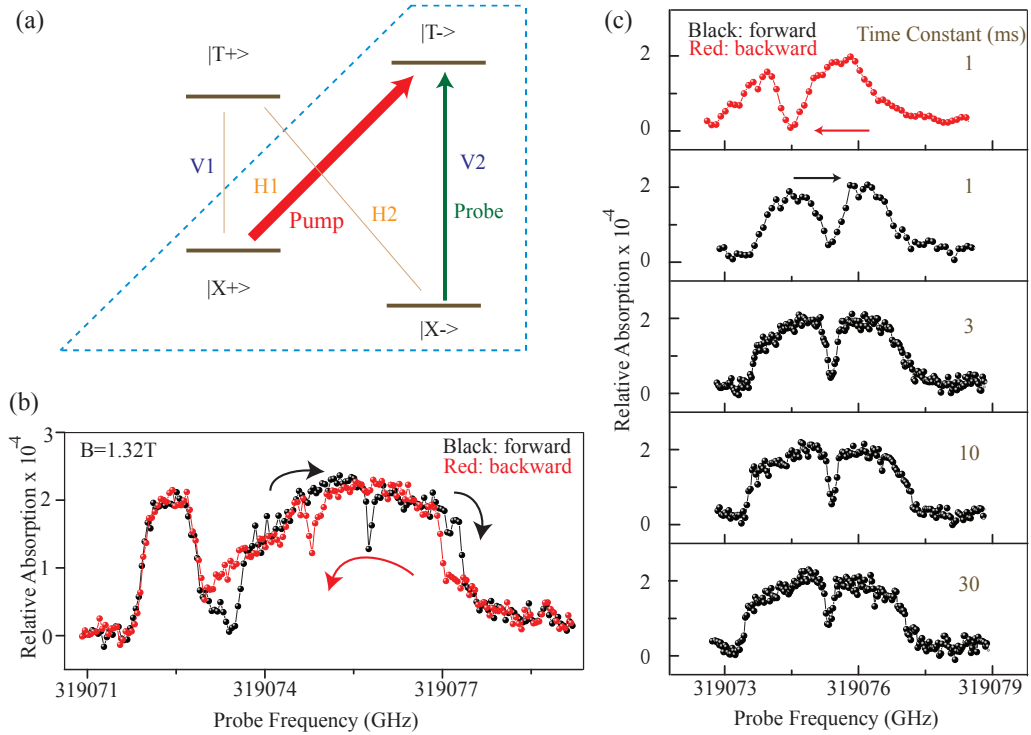
Figure 4.1: (a)Four level energy structure of the quantum dot with applied magnetic field of 1.32T in the Voigt geometry. The pump and probe lasers excite a three level Λ subsystem (dashed outline). The pump-probe laser geometry is reversed from chapter 3. (b) Probe absorption spectrum for both forward (red to blue) and backward (blue to red) scans. The peak on the red end of the spectrum corresponds to the the H2 transition. The V2 peak is distorted from the normal dark state lineshape. Hysteresis is evident at both the trailing edge and at the dark state dip. (c) Probe absorption spectra of transition V2 only. The probe scans faster with lower lock-in time constant. Faster scans show less lineshape distortion. Hysteresis is evident even at the fastest scan rate, with lock-in time constant 1ms.

The experiment is performed on the same single negatively charged quantum dot as in section 3.2.2 with an external magnetic field (1.32T) applied in the Voigt

geometry. In the pump-probe experiment, two narrow linewidth continuous wave (CW) lasers selectively excite a three level lambda (Λ) subsystem, as shown in the dashed box of Fig 4.1a. Note that the pump and probe have been reversed when compared to the experimental setup in Sec 3.2.2. The difference between the data presented here versus the experiment in Sec 3.2.2 is that the pump power is larger here. The pump intensity in Sec 3.2.2 ranges from a factor of 5 less to the minimum intensity used in this experiment. However, the same dark state physics applies and the theoretical discussion in section 3.2.2 is valid here as well. The pump and probe are orthogonally polarized and the pump is rejected before the detector by a polarization analyzer. A large AC voltage applied across the sample allows the use of Stark shift modulation to directly measure the absorption spectrum. Figure 4.1b shows the probe absorption spectrum. The black (red) curve is the spectrum obtained by scanning the probe laser from low (high) energy to high (low) energy, denoted in the figure as the forward (backward) scan. The narrow peak on the left and the broad peak on the right correspond to transitions H2 and V2, respectively. We will focus on the optical response from transition V2.

Ideally, the lineshape of transition V2 should be Lorentzian like with a dark state dip, as seen in section 3.2.2. The probe absorption spectrum in fig 4.1b is clearly distorted, showing a broadened lineshape with a round top and sharp edges. The dark state dip is also narrower and shallower than expected. More remarkably, we observe hysteresis at the sharp edges of the V2 absorption peak between the forward and backward scans. Additionally, the spectral position of the dark state is shifted in the same direction as the scan, which indicates a change of the two photon resonance (TPR) when the scan direction is switched. The TPR is equal to the electron spin Zeeman splitting, and is governed by the magnetic field along the x-axis. As the external magnetic field is unchanged in the forward and backward scans, these observations indicate that we optically create and probe a dynamic nuclear spin polarization (DNP), where the nuclear spin configuration depends on the laser scan direction.

We plot the absorption spectrum for different laser scan rates in Fig 4.1c . The scan

rate is given in terms of the lockin amplifier time constant, where a short (longer) time constant indicates a faster (slower) laser scan rate. The dark state becomes more pronounced and broader as we increase the laser scan rate (i.e. the probe laser frequency is held for a shorter time at each value). With faster scan speeds, the measured lineshape is closer to the standard dark state spectrum, such as seen in Sec 3.2.2. We posit that the anomalous spectral features and their scan-rate dependence reflect the dynamical control of the nuclear field by the laser frequency scans on a timescale comparable to the nuclear spin relaxation time (order of 1s [5–7]). For slower scan rates, the nuclear configuration changes with laser frequency, leading to alterations of the absorption lineshape.

4.2   Theory of the Hole Assisted Dynamic Nuclear Polarization Feedback Effect [1]

The complete electron-nuclear spin hyperfine interaction Hamiltonian has the form [9]:

$$H_{\text{nuc}} = \frac{-\mu_0}{4\pi}\gamma_N\gamma_e \sum_k \hat{I}_k. \left[\frac{8\pi}{3}\hat{S}\delta\left(\vec{r}_k\right) - \frac{r_k{}^2\hat{S} - 3\vec{r}_k\left(\hat{S}.\vec{r}_k\right)}{r_k{}^5} + \frac{\hat{L}}{r_k{}^3} \right] \qquad (4.1)$$

where γ_N and γ_e are, respectively, the nuclear and electron gyromagnetic ratios, $\vec{r}_k$ is the position of the electron from the kth nuclear spin. $\hat{S}$ and $\hat{L}$ are the spin and orbital angular momentum operators of the electron and $\hat{I}_k$ is the spin of the kth nucleus. The first term is called the Fermi contact hyperfine interaction, the second term corresponds to the dipole-dipole spin interaction and the third term is a coupling between the electron orbit and the nuclear spin, known as the chemical shift. The chemical shift is most notable in molecules and will be ignored here.

In Sec 2.2.2, we discovered that the electron spin ground state wavefunction is a product of a nearly spherical envelope with an s-orbital central cell wavefunction. Since the dipole-dipole interaction has odd parity, it is easy to see that the dominant term in the electron-hole hyperfine interaction is the Fermi contact interaction. The

[1]The discussion in this section follows the derivations by Wang Yao as given in Ref [8]

Hamiltonian is simplified to [8]

$$H_{e-n} = \sum_k A_{e,k} \left(S^x I_k{}^x + \frac{S^+ I_k{}^- + S^- I_k{}^+}{2} \right)$$

$$A_{e,k} = A_{e,\alpha_k} |f_e(\vec{R}_k)|^2 \frac{c_0{}^3}{4} \tag{4.2}$$

where $f_e(\vec{R}_k)$ is the normalized electron envelope wavefunction, c_0 is the lattice constant. $A_{e,\alpha}$ is the hyperfine coupling constant, where $A_{e,In} = 56\mu eV$ and $A_{e,As} = 46\mu eV$ [1, 10–12]. Each unit cell contains one As and one In atom, so if the total quantum dot volume is V, then the total number of nuclei in the dot is N=$8V c_0^{-3}$. The coupling between any nucleus and the electron is inversely proportional to N. The larger the dot, the more spread out the electron wavefunction and the less interaction there is with any given nucleus.

The first term in the Hamiltonian, proportional to $S^x I_k{}^x$, represents an additional Zeeman term[2], where a quantum mechanical time average over the x-component of the nuclear spins form an equivalent magnetic field (the Overhauser field) that shifts the electron spin energies. The Overhauser field B_N can be defined as [1]

$$B_N = \frac{c_0{}^3}{4} \frac{1}{\mu_B g_e} < \sum_k A_{e,\alpha_k} |f_e\left(\vec{R}_k\right)|^2 \hat{I}_k{}^x > \tag{4.3}$$

where g_e is the electron g-factor and ¡...¿ is an average over the nuclear ensemble.

If the nuclear spins are in a random, gaussian distribution, an average over a large number of electron spin measurements will show a decay in the electron spin coherence, with a characteristic decay time [1] γ_s

$$\gamma_s = \sqrt{\frac{16 \sum_j I^j (I^j + 1)(A^j)^2}{3\hbar N}} \tag{4.4}$$

where I^j is the spin of the jth nuclear spin, A^j is isotropic hyperfine constant, and N is the number of nuclear spins. For the dots in this thesis, it is estimate that N= 2.5×10^4 and $I_{In} = 9/2$, $I_{As} = 3/2$, $A_{In} = 56\mu eV$, and $A_{As} = 47\mu eV$ [10].

---

[2]Note that the external field is in the $\hat{x}$ direction.

Although gallium diffuses from the intrinsic layer into the quantum dot, the presence of gallium in the dot is ignored for the remainder of this discussion. This results in a spin coherence time T2* $(1/\gamma_s)$ of about 400ps.

The second term in Eq 4.2 is a spin flip term, $S^+ I_k^- + S^- I_k^+$, which flips a nuclear spin and an electron at the same time. In other systems, this electron mediated nuclear spin flip mechanism is cited as the cause of dynamical nuclear spin polarization (DNP) and plays a large role in electron spin dynamics [7, 13–16]. However, this interaction cannot explain the phenomena seen in the experiments here.

The nuclear Zeeman energy is in the 10's of MHz for a 1T external magnetic field while the electron Zeeman energy is about 7GHz. For the electron mediated spin flip to contribute to the nuclear spin dynamics in our system, the large energy mismatch must be compensated by phonons. This process is slow at cryogenic temperatures. Moreover, the thermal energy $k_B T$ is greater than the electron Zeeman splitting at 5K, so the phonon assisted process is equally efficient at flipping the electron up or down and leads to a background nuclear spin polarization that is proportional to the electron spin [8]. This interaction does not account for the hysteresis seen Fig 4.1b.

Instead, we look to the hole to explain the altered lineshape and the hysteresis effects. The hole's p-like central cell wavefunction (see Chapter 2) excludes the Fermi contact hyperfine interaction on symmetry principles, but allows the dipole-dipole interaction. Because the dipole-dipole interaction is long range, there is an interaction between the nuclei in one unit cell with the probability density of the hole in another unit cell in addition to the on-site interaction. It has been shown that this off-site interaction only leads to corrections on the order of 1% of the on-site interaction [11, 17], and will be ignored.

For the quantum dot under study, there is significant heavy hole -light hole mixing. The heavy hole states are defined such that $|S_h^z = 1/2\rangle \equiv |J_z = 3/2\rangle - \eta|J_z = -1/2\rangle$ and $|S_h^z = -1/2\rangle \equiv |J_z = -3/2\rangle - \eta|J_z = 1/2\rangle$, where the amount of mixing, η, about 0.2 in this dot, is determined by polarization dependant spectroscopy as in Chapter 3. The z-axis is taken to be the growth axis. If the envelope wavefunction varies slowly in the scale of one unit cell, the hole-nuclear hyperfine Hamiltonian reduces to [8]

$$H_{h-n} = \sum_k A_{h,k}(S^z I_k{}^z + O(\eta)(S^y I_k{}^y) + O(\eta^2)(S^x I_k{}^z + S^y I_k{}^z))$$

$$A_{h,k} = A_{h,\alpha_k} \| f_h(\vec{R}_k) \|^2 \frac{c_0^3}{4} \tag{4.5}$$

where f_h is the hole envelope wavefunction. According to experiment and calculations, $A_h \sim 0.1 - 0.2 A_e$ for both In and As [8].

Unlike the electron, there are anisotropic terms which couple the hole spin to the nuclear spin. Since the external magnetic field is in the $\hat{x}$ direction, we define the nuclear raising and lowering operators as $I_k^{\pm} = I_k^y \pm I_k^z$. Because of the anisotropic nature of the interaction, there are terms like $S^x I^{\pm}$ which can flip the nuclear spin without flipping the hole spin, unlike the electron case where the spin flip interaction came from terms of the form $S^{\pm} I^{\mp}$. If the field is entirely in-plane (in the xy plane), the spin flips come from the $O(\eta^2) S^x I_k{}^z$ term in the Hamiltonian. If there is an out-of-plane ($\hat{z}$) component of the external field, nuclear spin flips can arise from the $S^z I^z$ term as well.

The external field is assumed to be purely in-plane and we focus on the $S^x I^z$ term in Eq. 4.5. This flips the nuclear spin without flipping the hole spin, and costs only the nuclear Zeeman energy, which is on the order of 10MHz/Tesla. This is smaller than the homogeneous linewidth of the trion state and energy can be conserved without the need to invoke phonon assisted processes.

Because the laser scan rate and the dynamics of the nuclear spins is orders of magnitude slower than the optical interactions which drive the Λ system, the three level system is always in an instantaneous steady state, determined by the instantaneous laser detunings and the Overhauser field. $|\psi_i\rangle$ and $|\psi_f\rangle$ are the initial and final states of the trion system before and after a nuclear spin flip. The flip rate for the kth nuclear spin due to the $O(\eta^2) S_h^x I_k^{\pm}$ interaction can be calculated using Fermi's golden rule [8]

$$r_k^{\pm} \approx 2\pi \left| \langle \psi_f | O\left(\eta^2\right) A_{h,k} S_h{}^x I_k{}^{\pm} | \psi_i \rangle \right|^2 D\left(\pm \hbar \omega_N\right) \tag{4.6}$$

The total wavefunction is split into a direct product of the electronic state $|\psi^e\rangle$ and a nuclear state $|\psi^N\rangle$ so that

$$r_k^{\pm} \approx 2\pi \ O\left(\eta^4\right) A_{h,k}{}^2 \left|\langle\psi_f^e|S_h{}^x|\psi_i^e\rangle\right|^2 \left|\langle\psi_i{}^N|I_k{}^{\pm}|\psi_f{}^N\rangle\right|^2 D\left(\pm\hbar\omega_N\right) \qquad (4.7)$$

The electronic state $|\psi^e\rangle$ can be written in terms of the electron spin and hole states, $|\psi^e\rangle = a_+|+\rangle + a_-|-\rangle + a_T|T-\rangle$. The spin operator S_h^x only operates on the hole component and Eq 4.7 reduces to

$$r_k^{\pm} \approx \frac{\pi}{2}\rho_{t,i}\rho_{t,f}O\left(\eta^4\right) A_{h,k}{}^2 \left(j \pm m_k\right)\left(j \mp m_k + 1\right) D\left(\pm\hbar\omega_N\right) \qquad (4.8)$$

where $\rho_{t,i}(\rho_{t,f})$ is the initial (final) trion population, and m_k is the $\hat{x}$-component of the kth nuclear spin in the initial state. j=3/2 for As and 9/2 for In. r^+ (r^-) is the nuclear spin flip up (down) rate and $D(\pm\hbar\omega_N)$ is the density of the final states with nuclear Zeeman energy $\hbar\omega_N$. Equation 4.8 shows that the spin flip rate is proportional to the product of the initial and final trion populations, $\rho_{t,i}\rho_{t,f}$. However, because the initial population $(\rho_{t,i})$ is the same for both the flip up and the flip down process, it is clear that the faster process is one which results in a larger trion population, $\rho_{t,f}$. In other words, the hole assisted DNP process acts like a feedback mechanism to maximize the trion population.

To work more easily with the optical Bloch equations, the DNP rate equation is converted to an equation of motion for the Overhauser shift [8], Δ

$$\frac{d\Delta}{dt} = -\gamma_N\Delta + \alpha\rho_t\frac{\partial\rho_t}{\partial\delta} \qquad (4.9)$$

where the laser detuning, δ, is a function of the Overhauser shift, $\delta = \delta(\Delta)$. γ_N is the nuclear spin relaxation rate and α is a hyperfine coupling constant.

Figure 4.2a shows a simulated dark state spectrum in the absence of the hole assisted feedback mechanism. Figure 4.2b plots the $\rho_t\frac{\partial\rho_t}{\partial\delta}$ of the dark state spectrum, which is proportional to the DNP rate. The flip rate is positive to the red of the trion maxima and negative to the blue. The feedback effect acts much like the restoring force of a spring, with the trion maxima (the green circles in Fig 4.2b located at laser
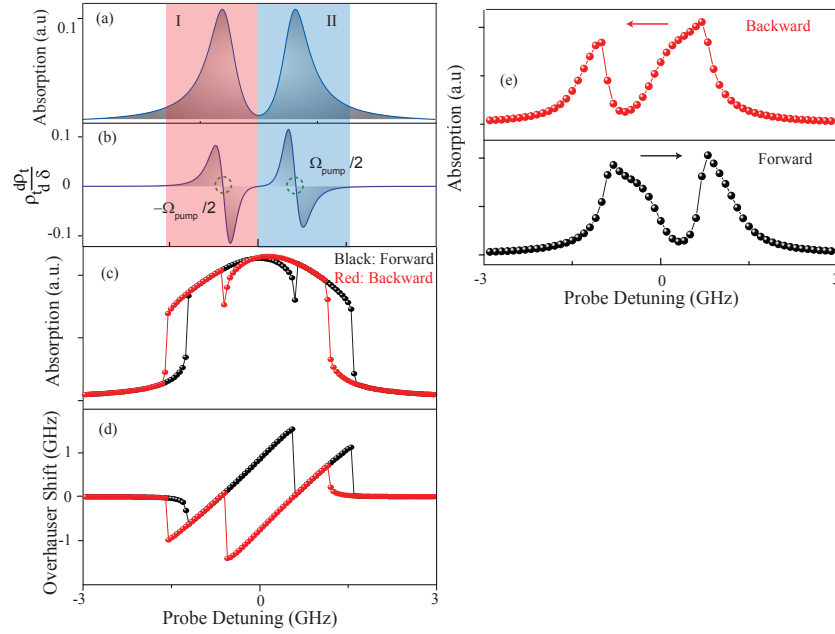
Figure 4.2: (a)A calculated dark state absorption spectrum in the absence of the hole assisted DNP effect. (b) A plot of $\rho_t \frac{\partial \rho_t}{\partial \delta}$ which is proportional to the spin flip rate. (c) Simulated absorption spectrum for a slow laser scan including the hole assisted DNP effect. (d) The Overhauser shift experienced by the electron spin, giving rise to the spectrum in (c). (e) Simulated absorption spectrum for a fast laser scan including the hole assisted DNP effect. Red lines indicate a forward scan direction and black lines indicate a backward scan direction.

detunings of $\delta = \pm \Omega_{pump}/2$) acting as stability points, were the flip rate goes to zero. When the laser detuning is shifted from the point of maximum trion excitation, the DNP feedback mechanism shifts the Overhauser field, and thus the Zeeman splittings, to maximize the excitation. This explains the distorted absorption lineshapes seen in Fig 4.1b.

Figure 4.2c simulates a slow laser scan including the DNP feedback effect [8]. This is done by solving the optical Bloch equations for a lambda system as in Sec 3.2.2 and replacing the probe detuning $\delta_{probe} = \omega_{laser} - \omega_t$ with $\delta_{probe} = \omega_{probe} - \omega_t - \Delta/2$, where δ_{laser} (δ_t) is the laser (trion) frequency and Δ is the Overhauser shift of the electron, governed by the equation of motion given by Eq 4.9. For the slow scan, the

scan is best reproduced using $\alpha = 2.4(MHz)^3$ and $\gamma_n = 1.5S^{-1}$.

The calculated Overhauser shift is plotted in Fig 4.2d. As the laser scans, the DNP feedback generates an Overhauser field to shift the TPR and pull the trion resonance toward the laser, creating sharp transitions while broading the absorption peaks. The Overhauser shift changes sign depending on the laser scan direction, creating a hysteresis between forward and backward scans. When the laser scans faster than the nuclei can flip, the lineshape more closely resembles a normal dark state absorption spectrum. This is simulated in Fig 4.2c using $\alpha = 50(MHz)^3$ and $\gamma_n = 2.5S^{-1}$ to best match the experimental data in Fig 4.1c.

4.3   Experimental Measurement of Dynamical Nuclear Polarization

We performed a set of measurements to show that the DNP maximizes the trion excitation by fixing the frequencies of both lasers and recording the optical response as a function of time. Figure 4.3a shows the probe absorption spectra with forward (black) and backward (red) scans where the magnetic field has been increased to 2.64T. We first scan the probe laser backward and stop the laser just before the sharp rising edge of the trion peak, as shown by the green curve in Fig 4.3b. We record the absorption signal as a function of time with the laser frequency fixed. As seen in Fig 4.3c, the system remains in hysteresis state 1 for a time (shown by the signal level) and abruptly switches into hysteresis state 2, where it remains. This signifies that the nuclear field switches to a stable value that maximizes the trion excitation. After waiting, we scan the probe laser forward and find that the subsequent partial forward scan spectrum (the blue curve in Fig 4.3d) overlaps considerably with its equivalent in the full forward scan.

The dynamics of the nuclear spin can also be examined by monitoring the dark state. After moving the pump laser slightly to the blue, we first take a forward scan to locate the dark state (black curve in Fig 4.3e), then take a partial forward scan to prepare the initial nuclear spin configuration and stop the laser just before the formation of the dark state (red curve). Immediately, the absorption signal is
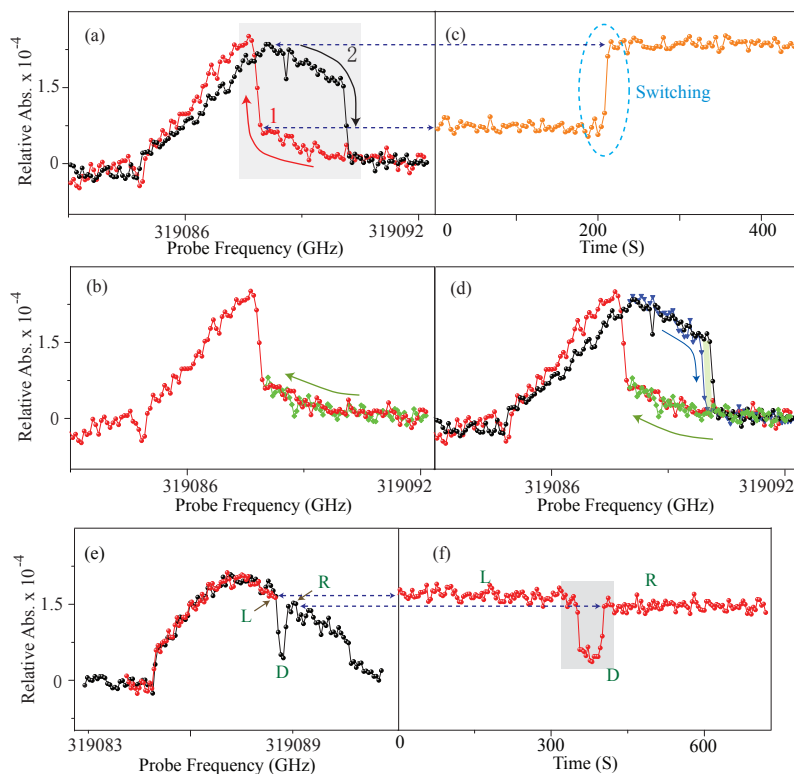
Figure 4.3: Data taken at a magnetic field of 2.64T (a) Black (red) curve is taken with a forward (backward) scan direction. (b) Green curve is a partial backward scan. (c) The probe absorption as a function of time immediate after stopping the laser just before the rising edge of the trion absorption. (d) A partial forward scan taken after the system switches hysteresis states. (e) The black (red) curve is a full (partial) forward scan. The labels L, D, and R denote three system configurations. (f) The probe absorption as a function time immediate after stopping the laser at L.

measured as a function of time (Fig 4.3f). From the signal level, we can tell that the system starts in configuration L, jumps into configuration D after some time, and then switches to configuration R, where it remains at a high probe absorption state. In experiments we noticed that the system can stay in the dark state D on a time scale from a few seconds to 3 minutes, indicating the meta-stable nature of the nuclear configuration at the TPR. Figure 2f shows an example where the system stays in the D configuration for 40s.

The metastablility of the dark state can be understood by the DNP rate shown

in Fig 4.2b. The two stable regions I and II lock the probe absorption to trion maxima,the points circled in green. The TPR is exactly between these two stability regions and is in fact an unstable point. However, the DNP rate is clearly zero at the TPR, and the slope of the DNP rate around the TPR is still small. So although the TPR is an unstable state for the DNP feedback mechanism, the dynamics at this point are slow as to make it metastable.

4.4   Nuclear Field Locking Enhances the Electron Spin Coherence Time

The self-locking effect described in the theory also leads to the suppression of the nuclear spin fluctuations. Once the system has switched to a configuration of maximum trion excitation, the electron spin Zeeman energy and hence the nuclear field are only determined and controlled by the instantaneous laser frequencies, regardless of the initial nuclear spin configuration before the scan starts. In this regime, the DNP feedback actively works to maximize the trion population. If the Overhauser field fluctuates, the Zeeman splitting changes, moving the trion transition slightly out of resonance with the laser. The DNP feedback effect immediately compensates for this shift and effectively dampens nuclear spin fluctuations (Fig 4.4a). Because nuclear fluctuations are main source of electron spin dephasing in this system, we should see an enhancement of the electron spin T2* time in the dark state absorption spectra.

Power dependent measurements of the dark state with a fast laser scan rate provide frequency domain information on the electron spin coherence time. Figure 4.4b shows the estimated spin decoherence rate decreases with the increase of the pump field strength (square root of the pump intensity). The black dots represent the electron spin dephasing rate, $\frac{\gamma_s}{2\pi}$, inferred from the absorption minimum at the dark state dip (normalized by the absorption maximum at the trion peak). When the pump Rabi frequency (Ω_{pump}) is large compared to the trion and spin dephasing times (γ_t and γ_s, respectively), the absorption, α, at the dark state dip and the Rabi side can be approximated as
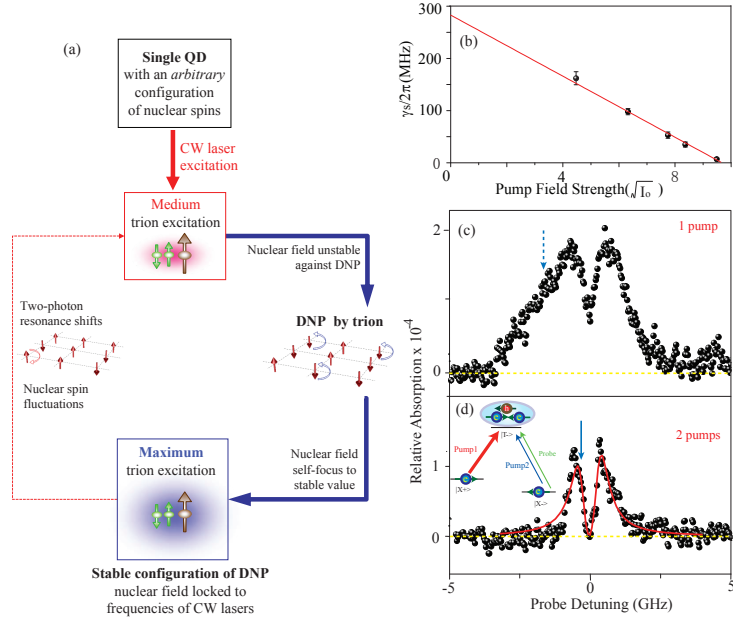
Figure 4.4: (a)Schematic of the DNP feedback mechanism. (b) Estimated electron spin decoherence rate $\left(\frac{\gamma_s}{2\pi}\right)$ from two beam absorption spectra. $I_0 = 2W\ cm^{-2}$. The black dots are rates inferred from absorption peak to dark state depth ratios while the triangles are values extracted from best-fit simulations. The dashed line is the thermal value of the decoherence rate at 5K. The red dot is the value from a fit of the three beam spectrum in (d). (b) An example of the spectra measured using a fast foward scan in the two beam geometry. (d) A three beam measurement taken using the laser geometry shown in the inset. The blue arrow indicates the position of pump 2. (Also the dashed arrow in (c) for reference).

$$\alpha_{dip} = \alpha_0 \frac{4\gamma_s}{\Omega_{pump}^2} \tag{4.10}$$

$$\alpha_{peak} = \alpha_0 \frac{1}{\gamma_t} \tag{4.11}$$

where α_0 is a constant. For our dot, we use $\gamma_t = 400 MHz$.

The blue triangles in Fig 4.4b are values extracted from the best fit of the dark state spectrum including the DNP dynamics[cite]. An example of the dark state spectrum is given in Fig 4.4c. For our dot, we estimate the spin inhomogeneous broadening due to a thermally distributed nuclear environment to be (360 ± 30) MHz. The dark state spectrum clearly shows that the spin T2* has been enhanced

to well above the thermal value.

The quantitative enhancement of T2* by the feedback mechanism is determined by the slope of the DNP rate as a function of detuning at the locking points, i.e. the two circled positions in Fig. 4.2b at $\pm\Omega_{pump}$. A larger slope means a stronger restoring force, and hence a better locking effect. As the pump power increases, the slope, and thus the restoring force increase as well.

For spectra discussed in Fig 4.3a and b, since the locking position of the nuclear field follows the probe laser, which scans much faster than the DNP equilibration rate, the suppression effect we obtained is a lower bound of the capability of this nuclear field locking technique. If the pump and probe beams are fixed spectrally to maximize the trion excitation, the electron spin T2* should be further enhanced. Data taken using three beams (laser geometry shown in Fig. 4.3d) support this argument.

The pump 1 remains near resonant with transition H1 and the pump 2 is tuned to transition V2 and fixed at the spectral position which maximizes the trion absorption. The two pumps lock the nuclear field and suppress nuclear fluctuations. We use the weak probe beam to measure the dark state spectrum with a fast scan rate, shown in Fig 4.4d. Since the probe is weak and scans at a fast rate, the effect of the probe beam on the nuclear field can be ignored.

The three beam spectrum in 4.4d shows a cleaner dark state lineshape with a more pronounced dip compared to the 2-beam spectrum in Fig 4.4c with comparable pump intensity. This confirms that the nuclear field is locked by the two pumps. Since the dip strength represents the electron spin T2* and the measured absorption at the TPR approaches zero, the data indicates a substantial enhancement of the T2* in this two-pump setup. It is challenging to extract an accurate spin decoherence rate since the suppression of nuclear spin fluctuations is so strong that the signal approaches zero at the TPR. However, fitting the data with the standard two beam optical Bloch equation (from Sec 3.2.2), the red curve on top of the data (using parameters $\Omega_{pump}/2\pi = 0.9 GHz, \gamma_t/2\pi = 0.4 GHz$ and $\delta_pump = -30 MHz$) yields $\gamma_s/2\pi$ on the order of 1 MHz with a 5 MHz upper bound error bar. We can also estimate the T2* directly from the absorption minimum at the dark state dip, though this will not

be as accurate as the optical Bloch equation curve fitting since it does not exploit all the data points. This dip-to-peak ratio estimation gives a $\gamma_s/2\pi$ of 2MHz, which agrees with the Bloch equation fit. The green curve on top of the data is a theoretical plot using the thermal value of T2* (360MHz at 5K), which clearly shows the strong enhancement of the electron spin T2* by the DNP self-locking effect.

4.5 Summary

In this chapter we explored the interaction of the hole spin with the nuclear spins that make up the quantum dot. The hole spin hyperfine interaction is a dipole-dipole interaction which has non-isotropic components that allow the flipping of the nuclear spin without flipping the hole spin. When lasers are applied in a dark state geometry, this interaction generates a feedback effect which maximizes the trion population via a dynamic nuclear spin polarization. This feedback effect can be used to control the average Overhauser field as well as suppress the nuclear spin fluctuations. We have been able to suppress the electron spin dephasing arising from nuclear spin fluctuations by over two orders of magnitude using this feedback mechanism. Although we have given a qualitative explanation for the suppression effect, there does not currently exist a microscopic theory which fully accounts for the two orders of magnitude suppression of electron spin dephasing that we have measured in this experiment.

BIBLIOGRAPHY

BIBLIOGRAPHY

[1] I. A. Merkulov, A. L. Efros, M. Rosen, "Electron spin relaxation by nuclei in semiconductor quantum dots", *Physical Review B* **65**, 205309 (2002).

[2] J. R. Petta, A. C. Johnson, J. M. Taylor, E. A. Laird, A. Yacoby, M. D. Lukin, C. M. Marcus, M. P. Hanson, A. C. Gossard, "Coherent Manipulation of Coupled Electron Spins in Semiconductor Quantum Dots", *Science* **309**, 2180 (2005).

[3] J. Baugh, Y. Kitamura, K. Ono, S. Tarucha, "Large Nuclear Overhauser Fields Detected in Vertically Coupled Double Quantum Dots", *Physical Review Letters* **99**, 096804 (2007).

[4] C. Lai, P. Maletinsky, A. Badolato, A. Imamoglu, "Knight-Field-Enabled Nuclear Spin Polarization in Single Quantum Dots", *Physical Review Letters* **96** (2006).

[5] A. Greilich, A. Shabaev, D. R. Yakovlev, A. L. Efros, I. A. Yugova, D. Reuter, A. D. Wieck, M. Bayer, "Nuclei-Induced Frequency Focusing of Electron Spin Coherence", *Science* **317**, 1896 (2007).

[6] P. Maletinsky, C. W. Lai, A. Badolato, A. Imamoglu, "Nonlinear dynamics of quantum dot nuclear spins", *Physical Review B (Condensed Matter and Materials Physics)* **75**, 035409 (2007).

[7] D. J. Reilly, J. M. Taylor, J. R. Petta, C. M. Marcus, M. P. Hanson, A. C. Gossard, "Suppressing Spin Qubit Dephasing by Nuclear State Preparation", *Science* **321**, 817 (2008).

[8] X. Xu, W. Yao, B. Sun, D. G. Steel, A. S. Bracker, D. Gammon, L. J. Sham, "Optically controlled locking of the nuclear field via coherent dark-state spectroscopy", *Nature* **459**, 1105 (2009).

[9] A. Abragam, *The Principles of Nuclear Magnetism*, Claredon Press, Oxford (1973).

[10] D. Paget, G. Lampel, B. Sapoval, V. I. Safarov, "Low field electron-nuclear spin coupling in gallium arsenide under optical pumping conditions", *Physical Review B* **15**, 5780 (1977).

[11] B. Eble, C. Testelin, P. Desfonds, F. Bernardot, A. Balocchi, T. Amand, A. Miard, A. Lemaitre, X. Marie, M. Chamarro, "Hole - Nuclear Spin Interaction in Quantum Dots", *0807.0968* (2008).

[12] P. Braun, X. Marie, L. Lombez, B. Urbaszek, T. Amand, P. Renucci, V. K. Kalevich, K. V. Kavokin, O. Krebs, P. Voisin, Y. Masumoto, "Direct Observation of the Electron Spin Relaxation Induced by Nuclei in Quantum Dots", *Physical Review Letters* **94**, 116601 (2005).

[13] D. Stepanenko, G. Burkard, G. Giedke, A. Imamoglu, "Enhancement of Electron Spin Coherence by Optical Preparation of Nuclear Spins", *Physical Review Letters* **96**, 136401 (2006).

[14] C. Latta, A. Hogele, Y. Zhao, A. N. Vamivakas, P. Maletinsky, M. Kroner, J. Dreiser, I. Carusotto, A. Badolato, D. Schuh, W. Wegscheider, M. Atature, A. Imamoglu, "Confluence of resonant laser excitation and bidirectional quantum-dot nuclear-spin polarization", *Nat Phys* **5**, 758 (2009).

[15] I. T. Vink, K. C. Nowack, F. H. L. Koppens, J. Danon, Y. V. Nazarov, L. M. K. Vandersypen, "Locking electron spins into magnetic resonance by electron-nuclear feedback", *0902.2659* (2009).

[16] H. Bluhm, S. Foletti, D. Mahalu, V. Umansky, A. Yacoby, "Enhancing the Coherence of a Spin Qubit by Operating it as a Feedback Loop That Controls its Nuclear Spin Bath", *Physical Review Letters* **105**, 216803 (2010).

[17] J. Fischer, W. A. Coish, D. V. Bulaev, D. Loss, "Spin decoherence of a heavy hole coupled to nuclear spins in a quantum dot", *0807.0386* (2008).

CHAPTER 5

Nuclear Spin Fluctuation Narrowing

In Chapter 4, we saw that the background nuclear spin bath can have a large effect on dynamics of the electron-trion system. Fluctuations of the nuclear spins lead to decoherence of the electron spin while hyperfine interactions between the nuclei and the hole spin can suppress nuclear fluctuations and increase electron spin coherence. The hole assisted feedback mechanism is not the only method to extend the electron spin coherence. In an ensemble of self assembled quantum dots, the ensemble decoherence of electron spins is dominated by the inhomogeneity of the electron spin g-factor so that the electrons precess at different frequencies (modes) in an external magnetic field. This dephasing mechanism can be overcome using a spin mode-locking technique [1]. This method has been used to extend the spin coherence (T2*) to $3\mu s$ and can even generate a single precession mode [2] where nearly the entire electron spin ensemble precesses with the same frequency. Ultrafast optical spin rotations have been performed on the single mode spin ensemble [3], treating the ensemble as a single qubit. This spin mode locking technique, while effective on ensembles, is not applicable to the single electron spin qubit in our experiments.

It is also possible to refocus or recover the electron spin coherence using spin echo or dynamical decoupling techniques [4–8]. By applying specifically designed pulse sequences (of which there are a variety), it is possible to reverse the decoherence of a single spin and increase the coherence time (T2*) to the intrinsic lifetime limit (T2). This has been achieve in electrically gated quantum dots and recently in a single self assembled quantum dot. However, this method requires that quantum
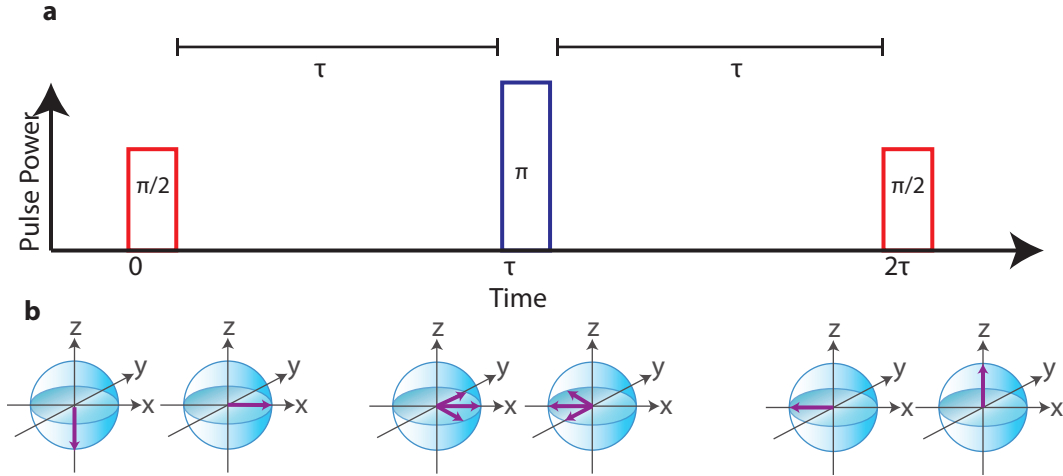
Figure 5.1: (a) Hahn echo sequence. The first pulse generates coherence. The second pulse rotates the spin by π at time t=τ. At t=2τ the spins rephase. (b) Bloch sphere diagram of the spins before and after each pulse in the Hahn echo sequence.

gate operations which are applied as part of a quantum calculation must be time to coincide with a rephased spin. For example, the Hahn echo [4] sequence for a two level system is illustrated in Fig 5.1a. The first $\pi/2$ pulse at t=0 simply rotates the population (arrow along z-axis in Fig 5.1b) into a coherence (the xy-plane). The state then decohereces. At $t = \tau$ a π pulse is applied and flips the spins. The spin coherence is revived at $t = 2\tau$ at which time a third pulse converts the coherence back into a population for readout. In this example, the quantum gate operation can only be applied at multiples of 2τ, to coincide with the refocused spin. This limits the duty cycle of quantum computations.

Due to the limitations of the above techniques, there has been considerable interest in suppressing electron spin dephasing directly by manipulating the nuclear spin ensemble [9–19]. This has been achieved to varying degree of success in both self assembled [9, 16] and gate defined quantum dots [14, 15, 17]. However, no other method has resulted in the two orders of magnitude enhancement of T2* that we have achieved using the hole assisted feedback effect. In this chapter, we will demonstrate that the hole assisted feedback mechanism can create nuclear spin narrowing

(NSN) prior to and separately from coherent electron spin manipulation necessary for spin qubit operations. We can greatly extend the number of qubit operations before the electron spin dephases while avoiding the timing complexities of spin echo and dynamical decoupling schemes.

5.1 Persistent Nuclear Spin Narrowing with Hole Assisted Dynamic Nuclear Polarization

We use the same dot and laser geometry as in Chapter 4. Two narrow bandwidth CW diode lasers selectively excite a three-level lambda (Λ) subsystem (Fig. 5.2a Inset). When the lasers are slightly detuned from the two-photon resonance (TPR) (pump 1 and pump 2 in Fig. 5.2a Inset), they create population in the excited trion state. The trion's unpaired hole interacts with the nuclei via a non-collinear hyperfine coupling [20], locking the Overhauser field and produces a nuclear spin narrowed state (NSN) via an intrinsic dynamic nuclear polarization (DNP) feedback process, as discussed in Chapter 4. When the lasers are tuned to the TPR (pump 1 and probe in Fig. 5.2a Inset), the laser coherence is imparted to the electron spin, forming a dark state which appears as a dip in the probe absorption spectrum. Dark state spectroscopy is used to read out the electron spin decoherence rate (1/T2*) [21]. Since nuclear spin fluctuations contribute significantly to T2*, dark state spectroscopy is a sensitive measure of NSN.

Using the feedback effect to generate NSN *during* a spin-based quantum computation can paradoxically decrease spin qubit coherence and fidelity. As shown in Chapter 4, the hole assisted feedback process maximizes trion population. This decreases electron spin population and contributes to the dephasing of the electron spin. To avoid this, we show that we can decouple NSN from electron spin control by passing all three lasers through acousto-optical shutters (Fig 5.2a) to individually gate the lasers and create NSN prior to generation and readout of the dark state, a coherent superposition of the electron spin states. The acousto-optical modulators are switched by MiniCircuits ZAS-3 switches, which are computer controlled via a
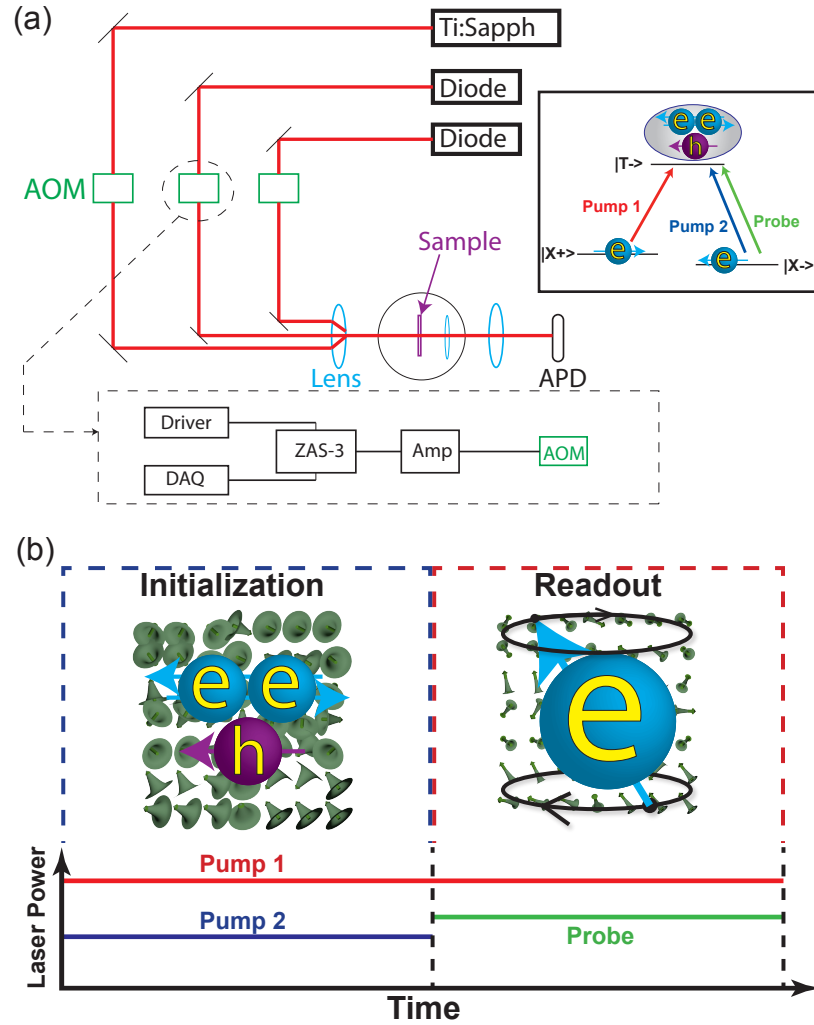
Figure 5.2: (a) Experimental arraignment to measure persistent nuclear spin narrowing using a three laser quasi-time domain measurement method. (Inset) Pump 1 is nearly resonant with transition H1, pump 2 and the probe are nearly resonant with transition V2. (c) Cartoon illustrating the laser illumination on the sample at each point in the scan. During the Initialization stage, pump 1 and pump 2 produce a trion, whose hole component interacts with the nuclear spins, preparing a NSN state. During the Read-out stage, pump 1 and the probe then produce and measure electron spin coherence, quantifying the narrowing of the nuclear spin distribution. The nuclear spins (green arrows in the background with large gaussian envelopes) start in a state of large fluctuation. The NSN state is represented by narrower gaussian envelopes, but maintains a similar average field.

National Instruments digital acquisition (DAQ) board. Figure 5.2b shows the gate timing diagram of the lasers at each point of the absorption spectrum (for example, the data points in Fig 5.3c) as the probe steps through the V2 resonance. At each point, pump 1 and pump 2 are first gated on, generating a hole which locks the Overhauser field and creates NSN ("Initialization" in Fig. 5.2b). Then, pump 2 is gated off and the probe is gated on for 25ms ("Read-out" in Fig. 5.2b) to measure the dark state spectrum and T2*.

An alternative to this interleaved method (where nuclear initialization and readout happens at every point in the absorption spectrum) is to initialize the NSN and then quickly scan the probe laser to measure the dark state so that initialization and readout only happen once per spectrum. However, unlike Chapter 4, the probe laser used in this experiment is a Coherent MBR 110 Ti:sapph laser. Unlike the 899-29, which can scan over 10GHz in 0.25s, this laser can only scan at a rate of 8GHz/s while maintaining a narrow linewidth. This slower scan rate would alter the lineshape and complicate the interpretation of the data. By interleaving, we can not only re-initialize the nuclei before every readout, but also decrease the readout time to arbitrarily small times, limited only by the lock in amplifier. In this case, the lock in amplifier integration time constant set to 5ms. The signal is only integrated during the read out phase to maintain a large signal strength.

We vary the initialization time to measure the onset of NSN. Figure 5.3a shows the measured probe absorption inside the dark state dip normalized to the absorption at the Rabi sidebands at sample temperatures of 5K (black curve) and 14K (red curve) and pump 1 (pump 2) Rabi frequency ($\Omega_R/2\pi$) of 700MHz(150MHz). Fitting the data to an exponential (solid lines), we extract an $1/e$ time of 7 ± 1ms at 5K and 12 ± 6ms at 14K.

Solving the optical Bloch equations for a strong pump and weak probe in the lambda system [21] (see Sec 3.2.2), we can find the probe absorption at the dark state dip (α_{dip}) and the Rabi sideband (α_{peak}) [20]

$$\alpha_{dip} = \alpha_0 \frac{\chi^2 \gamma_s + \gamma_t \left(\gamma_s{}^2\right)}{\chi^4 + 2\chi^2 \gamma_t \gamma_s + \gamma_t{}^2 \gamma_s{}^2} \tag{5.1}$$
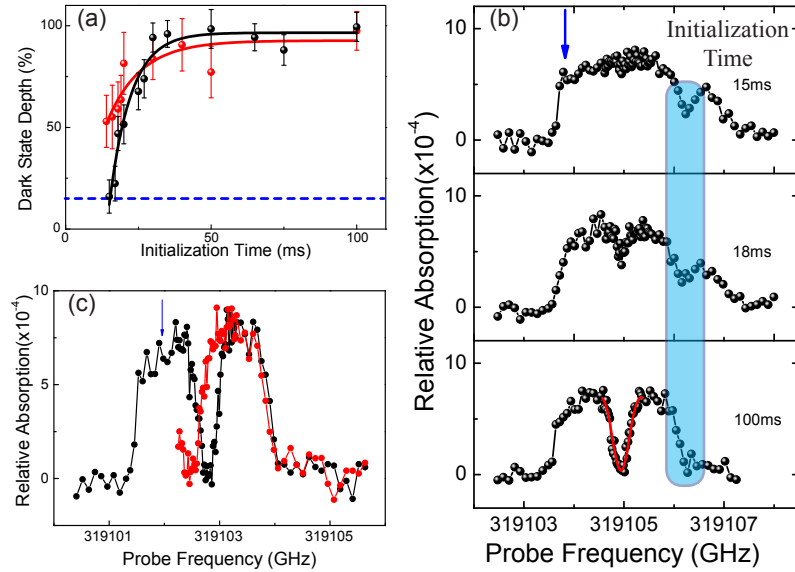
Figure 5.3: (a) Measured dark state depths (relative to the Rabi sidebands) as a function of the initialization time at sample temperatures of 5K (black) and 14K (red). The lines are fits to exponentials from which we can extract a $1/e$ time of 7 ± 1ms at 5K and 12 ± 6ms at 14K. The dashed blue line indicates the relative depth of the dark state for expected thermal value of the electron spin decoherence rate of 360MHz. (b) Absorption spectra corresponding to select points in (a). At short initialization times a second dip appears to the blue (highlighted in blue), indicating bistability of the Overhauser field. The red solid line is a fit to the optical Bloch equations. (c) The black spectrum is taken using a nominal scan range. The red spectrum has a reduced scan range and shows a corresponding shift of the TPR, due to probe effects on the Overhauser field. The blue arrows indicate the location of pump 2.

$$\alpha_{peak} = \alpha_0 \frac{\chi^2 \gamma_s + \gamma_t \left(\gamma_s{}^2 + \chi^2\right)}{2\chi^2 \gamma_t \gamma_s + \gamma_t{}^2 \gamma_s{}^2 + \left(\gamma_t{}^2 + \gamma_s{}^2\right)\chi^2} \tag{5.2}$$

where χ is half the pump 1 Rabi frequency, γ_t is the trion dephasing rate, γ_s is the electron spin dephasing rate, and α_0 is a constant. In the limit where $\gamma_s \ll \chi, \gamma_t$, the ratio between the dip and peak absorption reduces to $\frac{\alpha_{dip}}{\alpha_{peak}} \approx \frac{\gamma_t \gamma_s}{\chi^2}$. Using this method, we can estimate that $\gamma_s/2\pi = 7$MHz when the initialization time is 100ms (at 5K). We also fit the dark state portion of the spectrum (solid red line in Fig. 5.3b) with the optical Bloch equations [1] and find $\gamma_s/2\pi = 6$MHz. The expected thermal value of $\gamma_s/2\pi$ is 360MHz [20] at 5K and the relative dark state depth for this, calculated from simulations, is shown as the dashed blue line in Fig. 5.3a.

Figure 5.3b shows example spectra taken at 5K corresponding to several data points in Fig 5.3a, where the blue arrow represents the position of pump 2 and each figure is an average of 40 scans. Interestingly, at short initialization times, a second dip (highlighted in blue) appears about 1.3GHz to the blue of the central dark state dip. This is most likely caused by a bistability[2] of the Overhauser field [20,22,23] inducing a second TPR. Because the data is averaged, we expect that the bistability contributes to the weakening of the central dip. Thus, although we assume a simple exponential in Fig. 5.3a and extract $1/e$ times, the underlying physics which contribute to the form of the time dependance may be more complicated.

The measured onset time for NSN is less than the readout time; we are not completely successful in preventing the probe from perturbing the nuclei. This can be seen in the lineshapes of the absorption spectra in Fig. 5.3b and c, which do not correspond exactly to the expected dark state lineshape. Also, changing the starting position of the laser scan can shift the TPR, seen in the red curve in Fig. 5.3c, compared to the nominal scan range of the black curve. As the probe steps through the absorption spectrum, it will naturally create trion population in a small region

---

[1] The spectrum is too distorted to fit in its entirety. By fitting only the dip, we necessarily introduce error, as we are not exploiting all data points.

[2] From Chapter 4, we know that there are two stable values of the mean Overhauser field corresponding to the two Rabi sidebands of the dark state spectrum
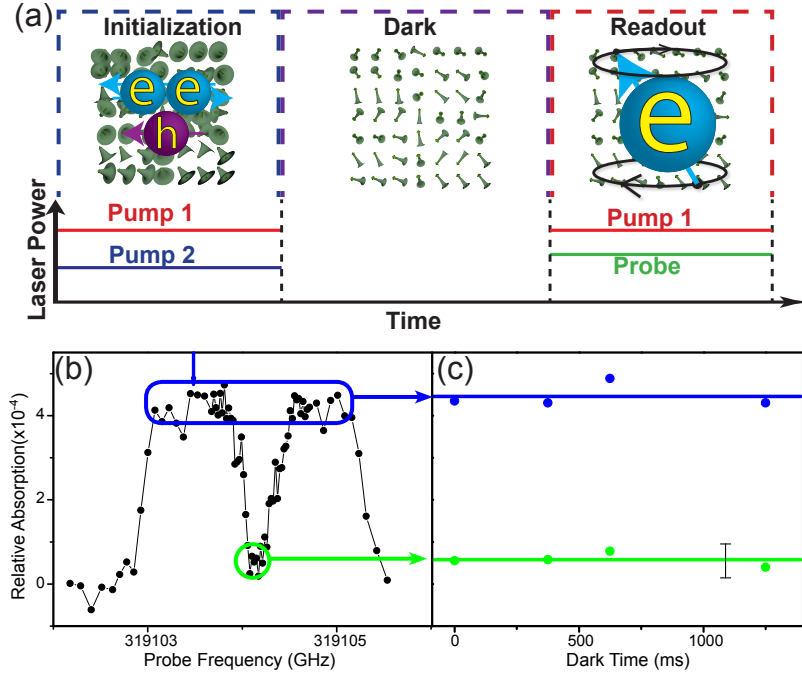
Figure 5.4: (a) We insert a dark period into the gating sequence to measure the persistence of the NSN as a function of laser dark time. (b) Absorption spectrum for 0ms dark time and a 62.5ms initialization time. Lines are guides to the eye. (c) The average absorption of the Rabi sidebands (blue) is plotted along with the absorption in the dark state dip (green) as a function of the dark time. Clearly, NSN persists in the absence of laser illumination for well over 1s. The solid lines are an average. The black I is the error bar.

around the absorption resonance. This causes the mean Overhauser field to shift via the hole assisted nuclear feedback effect. However, although the shift in the TPR illustrates that the average value of the Overhauser field has changed, the depth of the TPR dip has not changed, indicating that fluctuations were similarly suppressed in these two scans. Hence, the influence of the finite readout time does not impact our conclusion regarding the time scale of the preparation of the NSN state.

To measure the persistence of the NSN in the absence of laser interactions, we insert a dark period between the initialization and read out phases, indicated by the timing diagram in Fig. 5.4a. Using a pump 1 (pump 2) $\Omega_R/2\pi$ of 900MHz (650MHz) and an initialization time of 62.5ms, the absorption at both the dark state dip (green) and at the Rabi sidebands (blue) are plotted as a function of laser dark time in Fig.

5.4c. The dark state absorption does not change, showing that the NSN state persists when the lasers are shut off for a period of 1.25s (limited by the stability of the experimental apparatus) between preparation and readout. Additionally, the sample bias is still being modulated in accordance with the Stark shift modulation technique [24] (see Chapter 2) during this time. Because the modulation amplitude is large, the electron is shifted to an unstable point (co-tunneling region [25]) between the neutral exciton and trion bias regions [26] during one half-period of the modulation cycle. Thus, the electron is randomly reinitialized at a rate of at least 3.5KHz, corresponding to the modulation frequency. This shows that NSN appears to be insensitive to the electron charge and spin orientation and thus any quantum computation with the electron spin qubit should not affect the narrowed nuclear distribution [27]. The literature indicates that the narrowed nuclear spin distribution should persist from tens of seconds up to an hour [1, 14].

Interestingly, we have also found a combination of parameters which will initiate NSN with only a single laser. The inset of Figure 5.5a shows the timing diagram where only the pump 1 beam, with a Rabi frequency of $\sim$900MHz, is gated on during the initialization phase and then is turned off during the dark period. Using an initialization time of 50ms and a dark time of 300ms, the resulting probe absorption spectrum is shown in Figure 5.5a, and displays a deep dark state dip. If we remove the dark period and only initialize (Figure 5.5b Inset), the resulting spectrum (Figure 5.5b) displays a shallower dip shifted toward the blue. If instead, we remove the initialization phase (Figure 5.5c Inset) but keep the dark period, the spectrum also shows a shallow dip (Figure 5.5c) but further shifted toward the blue end of the spectrum. This is reminiscent of the 15ms and 18ms initialization time spectra shown in Figure 5.3b, where a similar dip appears to the blue of line center.

It is rather remarkable that this process can be initiated using a single laser beam. With the electron being refreshed at a rate of 3.5KHz, we expect pump 1 to resonantly create holes only about 175 times during each initialization, with optical pump rapidly eliminating the hole each time. We also anticipate the existence of background absorption from transitions originating in other parts of the sample
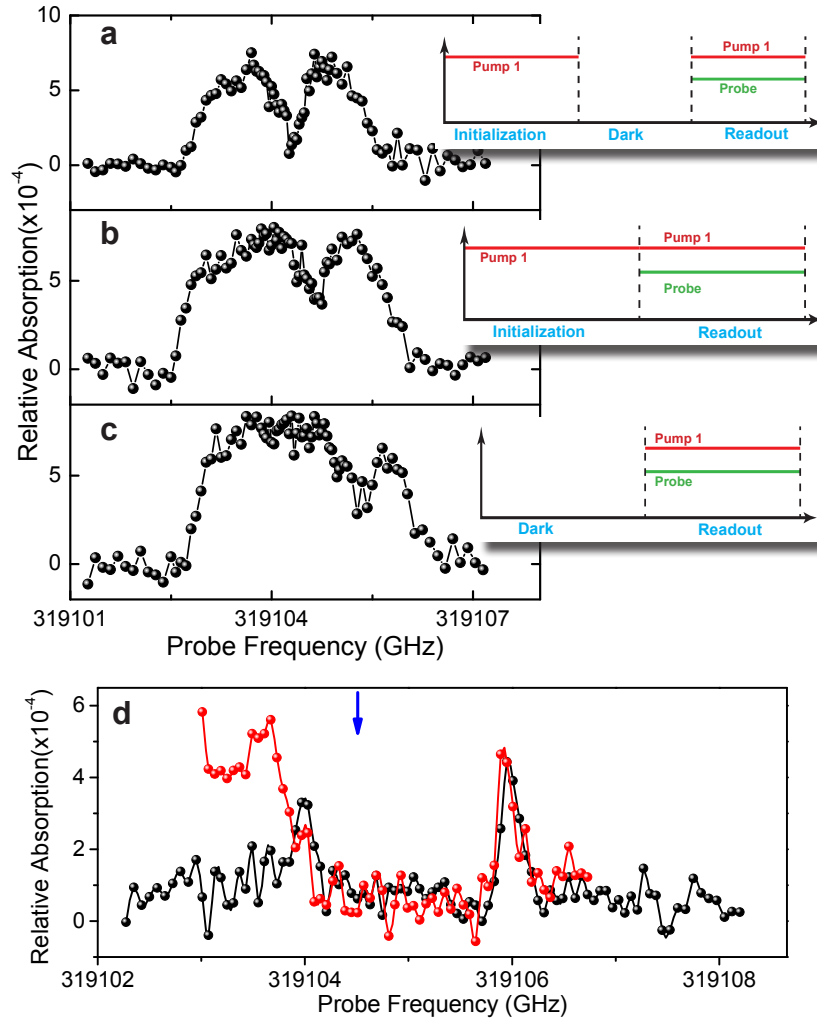
Figure 5.5: (a) Probe absorption spectrum with with pump 1 initializing for 50ms and a 300ms dark period which produces a NSN state. (b) Absorption spectrum with only a 300ms dark period prior to readout. (c) Absorption spectrum with pump 1 initializing for 50ms directly before read out. (d) All three lasers simultaneously illuminate the sample with no gating. The dark state follows the probe laser over a 2GHz region. The blue arrow is the pump 2 spectral position.

structure (eg. the wetting layer). If these transitions do not optically pump, then assuming that the lifetime is about 1ns, then there may be about 5×10^7 excitations of a hole during the 50ms of laser illumination. This background absorption would dominate the resonant process.

To test this hypothesis, we detuned the pump beam during the initialization stage by about -60GHz and see that we can still initialize the system (data not shown), indicating that indeed, there is some sort of background contribution to this single beam initialization. Although our understanding of the underlying physics is incomplete, it is clear that the dynamics must sitll be activated by the presence of the single pump beam and must evolve in time independent of optical interactions (although the electron is still modulated) to a point where the nuclear spin fluctuations are minimized. The NSN state is formed even when one leaves the laser on for the full 350ms(data not shown). This way, it is also possible to use pump 1 to initialize the *electron* spin via optical pumping [28] as well as read out the electron spin as in Ref [29] and Ref [30].

If we increase the pump powers and apply all three lasers at the same time without gating (Figure 5.5d inset), we find the probe can be used to continuously tune the Overhauser field (and thus the TPR). In Figure5.5d the pump 1 (pump 2) Rabi frequency has been increased to 1.5GHz (460MHz) and the blue arrow indicated the spectral position of pump 2. In the black spectrum, the two peaks are the outermost extents of the Rabi sidebands and the flat region in the middle is the TPR. The data shows that the Zeeman splitting of the spin states, as measured by the TPR, follows the probe frequency over a 2GHz region (consistent with theoretical simulations of the buildup of the Overhauser field in previous reports [20]) and the fluctuation suppression effect is maintained as the TPR is tuned. The red data is taken with the same experimental parameters as the black, but with a reduced scan. The large jumps at the low energy end of the red data is mostly likely an indication of Overhauser fluctuations, due to the probe scan starting in a region where the nuclear-hole interactions which lock the Overhauser field are just turning on.

5.2   Summary

In summary, we have shown that hole-assisted DNP feedback can be used to prepare the nuclear spins in a singly charged SAQD into a NSN state which can persist in the dark for over 1 second and has a preparation time of tens of milliseconds. The NSN depends only on the hole spin and is insensitive to the electron charge and spin orientation. This means that the NSN is decoupled from quantum gate operations in which pulsed lasers operate on the TPR. Because these pulses specifically avoid populating the excited state and act primarily on the spin ground states, they should have minimal impact on the NSN. This approach enhances the electron spin coherence prior to spin manipulation, thereby increasing the number of possible quantum computing operations without the need for spin echo coherence recovery or dynamic decoupling schemes.

BIBLIOGRAPHY

BIBLIOGRAPHY

[1] A. Greilich, A. Shabaev, D. R. Yakovlev, A. L. Efros, I. A. Yugova, D. Reuter, A. D. Wieck, M. Bayer, "Nuclei-Induced Frequency Focusing of Electron Spin Coherence", *Science* **317**, 1896 (2007).

[2] A. Greilich, S. Spatzek, I. A. Yugova, I. A. Akimov, D. R. Yakovlev, A. L. Efros, D. Reuter, A. D. Wieck, M. Bayer, "Collective single-mode precession of electron spins in an ensemble of singly charged (In,Ga)As/GaAs quantum dots", *Physical Review B* **79**, 201305 (2009).

[3] A. Greilich, S. E. Economou, S. Spatzek, D. R. Yakovlev, D. Reuter, A. D. Wieck, T. L. Reinecke, M. Bayer, "Ultrafast optical rotations of electron spins in quantum dots", *Nat Phys* **5**, 262 (2009).

[4] E. L. Hahn, "Spin Echoes", *Physical Review* **80**, 580 (1950).

[5] J. R. Petta, A. C. Johnson, J. M. Taylor, E. A. Laird, A. Yacoby, M. D. Lukin, C. M. Marcus, M. P. Hanson, A. C. Gossard, "Coherent Manipulation of Coupled Electron Spins in Semiconductor Quantum Dots", *Science* **309**, 2180 (2005).

[6] F. H. L. Koppens, K. C. Nowack, L. M. K. Vandersypen, "Spin Echo of a Single Electron Spin in a Quantum Dot", *Physical Review Letters* **100**, 236802 (2008).

[7] S. M. Clark, K. C. Fu, Q. Zhang, T. D. Ladd, C. Stanley, Y. Yamamoto, "Ultrafast optical spin echo for electron spins in semiconductors", *0904.0632* (2009).

[8] J. Du, X. Rong, N. Zhao, Y. Wang, J. Yang, R. B. Liu, "Preserving electron spin coherence in solids by optimal dynamical decoupling", *Nature* **461**, 1265 (2009).

[9] D. Stepanenko, G. Burkard, G. Giedke, A. Imamoglu, "Enhancement of Electron Spin Coherence by Optical Preparation of Nuclear Spins", *Physical Review Letters* **96**, 136401 (2006).

[10] G. Giedke, J. M. Taylor, D. D'Alessandro, M. D. Lukin, A. Imamogbrevelu, "Quantum measurement of a mesoscopic spin ensemble", *Physical Review A* **74**, 032316 (2006).

[11] D. Klauser, W. A. Coish, D. Loss, "Nuclear spin state narrowing via gate-controlled Rabi oscillations in a double quantum dot", *Physical Review B* **73**, 205302 (2006).

[12] M. S. Rudner, L. S. Levitov, "Self-Polarization and Dynamical Cooling of Nuclear Spins in Double Quantum Dots", *Physical Review Letters* **99**, 036602 (2007).

[13] J. Danon, Y. V. Nazarov, "Nuclear Tuning and Detuning of the Electron Spin Resonance in a Quantum Dot: Theoretical Consideration", *Physical Review Letters* **100**, 056603 (2008).

[14] D. J. Reilly, J. M. Taylor, J. R. Petta, C. M. Marcus, M. P. Hanson, A. C. Gossard, "Suppressing Spin Qubit Dephasing by Nuclear State Preparation", *Science* **321**, 817 (2008).

[15] I. T. Vink, K. C. Nowack, F. H. L. Koppens, J. Danon, Y. V. Nazarov, L. M. K. Vandersypen, "Locking electron spins into magnetic resonance by electron-nuclear feedback", *Nat Phys* **5**, 764 (2009).

[16] C. Latta, A. Hogele, Y. Zhao, A. N. Vamivakas, P. Maletinsky, M. Kroner, J. Dreiser, I. Carusotto, A. Badolato, D. Schuh, W. Wegscheider, M. Atature, A. Imamoglu, "Confluence of resonant laser excitation and bidirectional quantum-dot nuclear-spin polarization", *Nat Phys* **5**, 758 (2009).

[17] H. Bluhm, S. Foletti, D. Mahalu, V. Umansky, A. Yacoby, "Enhancing the Coherence of a Spin Qubit by Operating it as a Feedback Loop That Controls its Nuclear Spin Bath", *Physical Review Letters* **105**, 216803 (2010).

[18] W. A. Coish, J. Fischer, D. Loss, "Free-induction decay and envelope modulations in a narrowed nuclear spin bath", *Physical Review B* **81**, 165315 (2010).

[19] W. Yang, L. J. Sham, "Collective Nuclear Stabilization by Optically Excited Hole in Quantum Dot", *1012.0060v2* (2010).

[20] X. Xu, W. Yao, B. Sun, D. G. Steel, A. S. Bracker, D. Gammon, L. J. Sham, "Optically controlled locking of the nuclear field via coherent dark-state spectroscopy", *Nature* **459**, 1105 (2009).

[21] X. Xu, B. Sun, P. R. Berman, D. G. Steel, A. S. Bracker, D. Gammon, L. J. Sham, "Coherent population trapping of an electron spin in a single negatively charged quantum dot", *Nat Phys* **4**, 692 (2008).

[22] P. Maletinsky, C. W. Lai, A. Badolato, A. Imamoglu, "Nonlinear dynamics of quantum dot nuclear spins", *Physical Review B (Condensed Matter and Materials Physics)* **75**, 035409 (2007).

[23] A. I. Tartakovskii, T. Wright, A. Russell, V. I. Fal'ko, A. B. Van'kov, J. Skiba-Szymanska, I. Drouzas, R. S. Kolodka, M. S. Skolnick, P. W. Fry, A. Tahraoui, H. Liu, M. Hopkinson, "Nuclear Spin Switch in Semiconductor Quantum Dots", *Physical Review Letters* **98**, 026806 (2007).

[24] B. Alen, F. Bickel, K. Karrai, R. J. Warburton, P. M. Petroff, "Stark-shift modulation absorption spectroscopy of single quantum dots", *Applied Physics Letters* **83**, 2235 (2003).

[25] M. Atature, J. Dreiser, A. Badolato, A. Hogele, K. Karrai, A. Imamoglu, "Quantum-Dot Spin-State Preparation with Near-Unity Fidelity", *Science* **312**, 551 (2006).

[26] R. J. Warburton, C. Schaflein, D. Haft, F. Bickel, A. Lorke, K. Karrai, J. M. Garcia, W. Schoenfeld, P. M. Petroff, "Optical emission from a charge-tunable quantum ring", *Nature* **405**, 926 (2000).

[27] Z. Gong, Z.-q. Yin, L. M. Duan, "Dynamics of Overhauser Field under nuclear spin diffusion in a quantum dot", *0912.4322* (2009).

[28] X. Xu, Y. Wu, B. Sun, Q. Huang, J. Cheng, D. G. Steel, A. S. Bracker, D. Gammon, C. Emary, L. J. Sham, "Fast Spin State Initialization in a Singly Charged InAs-GaAs Quantum Dot by Optical Cooling", *Physical Review Letters* **99**, 097401 (2007).

[29] D. Press, T. D. Ladd, B. Zhang, Y. Yamamoto, "Complete quantum control of a single quantum dot spin using ultrafast optical pulses", *Nature* **456**, 218 (2008).

[30] E. D. Kim, K. Truex, X. Xu, B. Sun, D. G. Steel, A. S. Bracker, D. Gammon, L. J. Sham, "Fast Spin Rotations by Optically Controlled Geometric Phases in a Charge-Tunable InAs Quantum Dot", *Physical Review Letters* **104**, 167401 (2010).

CHAPTER 6

Summary and Future Directions

6.1 Summary

This thesis explored the energy level structure of single, neutral and singly charged quantum dots using coherent optical methods in the frequency domain. The InAs self assembled quantum dots used in this thesis where grown in a GaAs heterostructure, and form from a Stranski-Krastanow growth mode where the lattice mismatch between InAs and GaAs cause InAs droplets to form during growth. These droplets then become our quantum dots. Theoretical works by other researchers predict that the energy level structure inside these dots are discrete, and that electrons in the dot should be considered s-like in symmetry (L=0) while holes are p-like (L=1). Furthermore, the hole wavefunction is primarily of the heavy hole nature, the hole states are $|J = 3/2, j_z = \pm 3/2\rangle$ when we consider the spin-orbit interaction. Our frequency domain pump-probe spectroscopy of a neutral quantum dot shows that it maintains it's discrete energy level structure even in the presence of intense optical pumping. The three level V-system of the neutral exciton exhibits Autler-Townes splitting when the pump and probe couple separate legs of the V-system while we see the Mollow absorption spectrum when the pump and probe excite the same transition. These spectra are fully predicted by simple three and two level density matrix calculations, indicating that the quantum dot is well isolated from the complex many body behavior in bulk material. Furthermore, we can calculate the optical dipole moment of the exciton transition by measuring the Rabi splitting in the Autler-Townes and Mollow

absorption spectra. The dipole moment is a measure of the interaction strength between the optical field and the exciton transition and quantum dots with large dipole moments can be manipulated using less optical power.

Proceeding to the quantum information processing aspect of our work, we then charged a single quantum dot with a single electron. This is accomplished by applying a bias voltage across the Schottky diode structure that the dot is embedded in. With a single electron as the ground state, the excited state is a trion, a charged exciton. The spin pairing of the electrons in the excited states eliminates the anisotropic exchange splitting, resulting in two degenerate two level systems, each with orthogonal circular polarized transitions. In order to optically couple the two spin states, we turn on a magnetic field in the Voigt geometry, perpendicular to the growth direction. This splits and mixes the spin states, turning on the spin flip Raman transitions. The singly charged dot is now a four level system.

We focus on a three level lambda (Λ) subsystem. When a single laser is resonant with one of the transitions, population can be pumped from one spin state to the other on a fast timescale. This serves as a fast spin initialization procedure for quantum computing applications; the pumping rate can be on the order of GHz. When a second laser is placed on the other leg of the lambda system, the coherence of the lasers is imparted into the electron spin, forming a coherent superposition of the spin states through coherent population trapping. Whereas a single laser can initialize the electron to a single spin state, coherent population trapping can initialize the spin into an arbitrary superposition state by changing the ratio of the laser powers.

Because the dark state formed by coherent population trapping is a superposition state, it is very sensitive to coherence of the electron spin. The dark state absorption spectrum of the probe laser can be used to measure the decoherence rate of the electron spin. This is an important figure of merit, as current consensus indicates that fault tolerant quantum computing may require $10^4 - 10^5$ qubit operators before the state decoheres. Using dark state spectroscopy, we have measured the decoherence rate to be about 40MHz.

The source of this decoherence is primarily due to the fluctuations in the sur-

rounding nuclear spin bath, composed by the indium and arsenic atoms which make up the dot. The hyperfine coupling between the single electron spin and the 10^4 nuclear spins cause each nuclear spin flip to subtly change the electron spin splitting. A time average over the ensemble leads to fast dephasing of the electron spin. We have found, through dark state spectroscopy, an interaction between the hole spin and the nuclei which leads to a feedback process that locks the average nuclear magnetic field (Overhauser field) to a value controlled by the laser detuning. Not only can this locking effect be used to control the Overhauser field, but it also suppresses the fluctuations of the nuclear spins. The statistical distribution of nuclear magnetic field values is considerably narrowed, leading to a measured 1MHz electron spin dephasing rate while the nuclear field is locked. This is two order of magnitude lower than the thermal dephasing rate, calculated to be about 360MHz.

We have found that this impressive feat of prolonging the electron spin coherence can persist even after the optical fields are turned off. The narrowed nuclear spin distribution can be created in only 10's of milliseconds and persists in the dark for well over 1s, longer than the intrinsic decay time of the electron spin. Furthermore, we find that the nuclear spin narrowed state is insensitive to the dynamics of the electron spin. Charging of the quantum dot and fluctuations of the electron spin polarization while the optical fields are off do not impact the persistence of the nuclear spin narrowed states. We can now conceive of a procedure for quantum information processing whereby we first calm the nuclear spin fluctuations using this method. Subsequent electron spin qubit rotations which do not generate significant trion population can be done achieved without the need to resort to complicated spin echo or dynamical decoupling schemes which can rephase the qubit only at certain time intervals.

6.2   Future Directions

In this section, I will discuss some possible future experiments based on the results in this thesis.

6.2.1 Maximizing Qubit Rotations in a Single Quantum Dot

The most obvious extension of the work in this thesis is to combined the nuclear spin narrowing with time domain single qubit gates. Coherent rotations of a single electron spin in a self assembled quantum dot has been achieved using detuned optical pulses acting on the two photon resonance [1, 2]. A continuous wave laser placed on one of the legs of the lambda system acts to both initialize the spin state via optical pumping and acts as an optical tripwire to read the spin state after the rotations have been completed. As the pulse repetition rate is about 80Mhz, the CW laser can fully initialize the system between each pulse set with an optical pumping rate of about 1GHz.

Due to spin decoherence, one can only complete a finite number of spin rotations. The idea then is to integrate the hole assisted feedback mechanism with the gate operations. Because the detuned optical pulses should only act on the electron spin, there should be minimal hole population and thus the spin rotations should have minimal effect on the NSN state. The purposes of this experiment is to confirm the compatability between NSN and detuned optical control pulses. This can be done by first using the two CW lasers, slightly detuned from the two photon resonance, to generate hole population and create NSN. This should take on the order of 10s of milliseconds. Next, one of the CW lasers is gated off initialize the electron spin state. Since the initialization rate is fast (1GHz) this can be done very quickly and adds little overhead to the computation. Next, we generate a spin coherence using an optical pulse and let that coherence precess in the magnetic field. We use a delayed second pulse to rotate the coherence back into a population, which can be read out by a CW laser. The experiment is performed in a similar way to Refs [1, 2] only with very long delay times. The measured dephasing of the electron spin should be considerably longer with the NSN.

6.2.2 Quantum Dot Molecules

As we mentioned in Chapter 2, InAs quantum dots are highly strained. This strain

can propagate through bulk material and a second quantum dot layer grown above the first will nucleate the self assembly process and form a second layer of dots aligned to the first. If the layers are close enough, and if the electron wavefunctions have enough overlap, this growth process can form quantum dot molecules [3–6] with each dot charged with one electron. This entangles the two qubits and recent experiments have shown that it is possible to optical control the entangled qubits, creating a two qubit phase gate [6]. It is currently speculated that internal charge fluctuations have the greatest contribution to dephasing in this system, however there have not been any measurements of nuclear interactions thus far. It would be beneficial to measure the dephasing processes and see what effects, if any, the nuclei have on the entangled electron spins.

In summary, this thesis has presented new results in the area of spin based quantum computing in self assembled quantum dots. We have met many important milestones and identified new physics which may be instrumental in the development of practical quantum computing in self assembled quantum dots.

BIBLIOGRAPHY

BIBLIOGRAPHY

[1] D. Press, T. D. Ladd, B. Zhang, Y. Yamamoto, "Complete quantum control of a single quantum dot spin using ultrafast optical pulses", *Nature* **456**, 218 (2008).

[2] E. D. Kim, K. Truex, X. Xu, B. Sun, D. G. Steel, A. S. Bracker, D. Gammon, L. J. Sham, "Fast Spin Rotations by Optically Controlled Geometric Phases in a Charge-Tunable InAs Quantum Dot", *Physical Review Letters* **104**, 167401 (2010).

[3] M. F. Doty, M. Scheibner, A. S. Bracker, I. V. Ponomarev, T. L. Reinecke, D. Gammon, "Optical spectra of doubly charged quantum dot molecules in electric and magnetic fields", *Physical Review B (Condensed Matter and Materials Physics)* **78**, 115316 (2008).

[4] D. Kim, S. E. Economou, S. C. Badescu, M. Scheibner, A. S. Bracker, M. Bashkansky, T. L. Reinecke, D. Gammon, "Optical Spin Initialization and Nondestructive Measurement in a Quantum Dot Molecule", *Physical Review Letters* **101**, 236804 (2008).

[5] M. F. Doty, J. I. Climente, A. Greilich, M. Yakes, A. S. Bracker, D. Gammon, "Hole-spin mixing in InAs quantum dot molecules", *Physical Review B* **81** (2010).

[6] D. Kim, S. G. Carter, A. Greilich, A. S. Bracker, D. Gammon, "Ultrafast optical control of entanglement between two quantum-dot spins", *Nat Phys* **7**, 223 (2011).

APPENDICES

APPENDIX A

Calculating the Autler-Townes Spectrum

The Hamiltonian for the V-system is given by

$$\begin{pmatrix} \delta\text{p} & \chi\text{p} & 0 \\ \chi\text{p} & 0 & \chi\text{d} \\ 0 & \chi\text{d} & \delta\text{d} \end{pmatrix} \tag{A.1}$$

where χ_p one half the probe Rabi frequency where χ_d is one half the pump Rabi frequency. The pump and probe detunings are given by δ_d and δ_p respectively. The decay is given by the matrix

$$\begin{pmatrix} -\Gamma\rho_{11} & -\gamma\rho_{12} & -\gamma31\ \rho_{13} \\ -\gamma\rho_{21} & \Gamma\rho_{11} + \Gamma\rho_{33} & -\gamma\rho_{23} \\ -\gamma31\rho_{31} & -\gamma\rho_{32} & -\Gamma\rho_{33} \end{pmatrix} \tag{A.2}$$

The equation of motion for the density matrix is given by

$$i\frac{d\rho}{dt} = [H, \rho] + Decay \tag{A.3}$$

To calculated the probe response using perturbation theory, we replace $\rho \rightarrow \overset{0}{\rho} + \overset{1}{\rho} + ...$ and $H \rightarrow \overset{0}{H} + \overset{1}{H}$ where $\overset{0}{H}$ includes only the pump term and $\overset{1}{H}$ includes only the probe term. To zeroeth order of the probe, the equations are
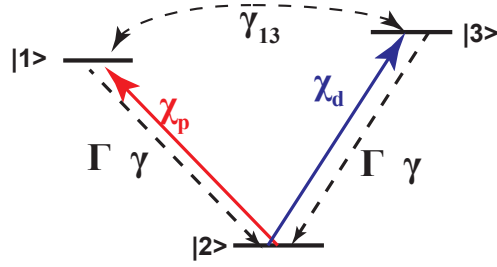
Figure A.1: V-System Energy Diagram. χ_p is the probe beam, χ_d is the pump beam. Γ is the population decay rate and γ is the transition dephasing rate. γ_{13} is the dephasing rate between the two excited states.

$$-i\Gamma\overset{0}{\rho}_{11} = 0 \tag{A.4}$$

$$(-i\gamma + \delta\mathrm{p})\overset{0}{\rho}_{12} - \chi\mathrm{d}\overset{0}{\rho}_{13} = 0 \tag{A.5}$$

$$-\chi\mathrm{d}\overset{0}{\rho}_{12} + (-i\gamma 31 - \delta\mathrm{d} + \delta\mathrm{p})\overset{0}{\rho}_{13} = 0 \tag{A.6}$$

$$(-i\gamma - \delta\mathrm{p})\overset{0}{\rho}_{21} + \chi\mathrm{d}\overset{0}{\rho}_{31} = 0 \tag{A.7}$$

$$-\chi\mathrm{d}\overset{0}{\rho}_{23} + \chi\mathrm{d}\overset{0}{\rho}_{32} + i\Gamma\left(\overset{0}{\rho}_{11} + \overset{0}{\rho}_{33}\right) = 0 \tag{A.8}$$

$$-\chi\mathrm{d}\overset{0}{\rho}_{22} + (-i\gamma - \delta\mathrm{d})\overset{0}{\rho}_{23} + \chi\mathrm{d}\overset{0}{\rho}_{33} = 0 \tag{A.9}$$

$$\chi\mathrm{d}\overset{0}{\rho}_{21} + (-i\gamma 31 + \delta\mathrm{d} - \delta\mathrm{p})\overset{0}{\rho}_{31} = 0 \tag{A.10}$$

$$\chi\mathrm{d}\overset{0}{\rho}_{22} + (-i\gamma + \delta\mathrm{d})\overset{0}{\rho}_{32} - \chi\mathrm{d}\overset{0}{\rho}_{33} = 0 \tag{A.11}$$

$$\overset{0}{\rho}_{11} + \overset{0}{\rho}_{22} + \overset{0}{\rho}_{33} = 1 \tag{A.12}$$

giving the zeroeth order solution

$$\overset{0}{\rho}_{22} = 1 - \frac{2\gamma\chi d^2}{\gamma^2\Gamma + \Gamma\delta d^2 + 4\gamma\chi d^2} \tag{A.13}$$

$$\overset{0}{\rho}_{11} = 0 \tag{A.14}$$

$$\overset{0}{\rho}_{23} = -\frac{-i\gamma\Gamma\chi d + \Gamma\delta d\chi d}{\gamma^2\Gamma + \Gamma\delta d^2 + 4\gamma\chi d^2} \tag{A.15}$$

$$\overset{0}{\rho}_{32} = -\frac{i\gamma\Gamma\chi d + \Gamma\delta d\chi d}{\gamma^2\Gamma + \Gamma\delta d^2 + 4\gamma\chi d^2} \tag{A.16}$$

$$\overset{0}{\rho}_{33} = \frac{2\gamma\chi d^2}{\gamma^2\Gamma + \Gamma\delta d^2 + 4\gamma\chi d^2} \tag{A.17}$$

$$\overset{0}{\rho}_{12} = 0 \tag{A.18}$$

$$\overset{0}{\rho}_{13} = 0 \tag{A.19}$$

$$\overset{0}{\rho}_{21} = 0 \tag{A.20}$$

$$\overset{0}{\rho}_{31} = 0 \tag{A.21}$$

To solve for the first order in the probe, the equation of motion is given by $[\overset{0}{H}, \overset{1}{\rho}] + [\overset{1}{H}, \overset{0}{\rho}]$. In the Maxwell Bloch formulation, the probe absorption is given by $-Im[\rho_12]$. After solving the first order equations, we find

$$\overset{1}{\rho}_{12} = \frac{(-i\gamma 31 - \delta d + \delta p)\chi p \overset{0}{\rho}_{22} + \chi d\chi p \overset{0}{\rho}_{23}}{(i\gamma 31 + \delta d - \delta p)(-i\gamma + \delta p) + \chi d^2} \tag{A.22}$$

APPENDIX B

Calculating the Mollow Absorption Spectrum

The Mollow absorption spectrum can be calculated in the two level atom for a strong pump with Rabi frequency Ω_1 and a weak probe (Ω_2). The Hamiltonian is

$$H = \hbar \begin{pmatrix} 0 & \chi_1 e^{it\omega_1} + \chi_2 e^{it\omega_2} \\ \chi_1 e^{-it\omega_1} + \chi_2 e^{-it\omega_2} & \omega_0 \end{pmatrix} \tag{B.1}$$

where the ground state is at zero energy, the excited state is at energy $\hbar\omega_0$, the pump frequency is ω_1 and the probe frequency is ω_2 and $\chi = \Omega/2$. The decay matrix is given by

$$\begin{pmatrix} \Gamma\rho_{22} & -\gamma\rho_{12} \\ -\gamma\rho_{21} & -\Gamma\rho_{22} \end{pmatrix} \tag{B.2}$$

Next, we switch to the field interaction picture of the pump, where $\rho_{12} \to e^{i\omega_1 t}\tilde{\rho_{12}}$ and $\rho_{21} \to e^{-i\omega_1 t}\tilde{\rho_{21}}$. For simplicity, we define $\Delta = \omega_1 - \omega_0$ and $\delta = \omega_2 - \omega_1$. The master equation for the density matrix in the interaction picture [1] is given by $\frac{-i}{\hbar}([H,\rho] + decay)$ is

---

[1]We have removed the ˜ above the density matrix elements for clarity

$$\frac{\partial \rho_{11}}{\partial t} = \hbar \left(i\Gamma\rho_{22} - \rho_{12}\chi_1 + \rho_{21}\chi_1\right) - e^{-it\delta}\hbar\rho_{12}\chi_2 + e^{it\delta}\hbar\rho_{21}\chi_2 \tag{B.3}$$

$$\frac{\partial \rho_{12}}{\partial t} = \hbar \left(-i\gamma\rho_{12} + \Delta\rho_{12} - \rho_{11}\chi_1 + \rho_{22}\chi_1\right) - e^{it\delta}\hbar\left(\rho_{11} - \rho_{22}\right)\chi_2 \tag{B.4}$$

$$\frac{\partial \rho_{21}}{\partial t} = \hbar \left(-i\gamma\rho_{21} - \Delta\rho_{21} + \rho_{11}\chi_1 - \rho_{22}\chi_1\right) + e^{-it\delta}\hbar\left(\rho_{11} - \rho_{22}\right)\chi_2 \tag{B.5}$$

$$\frac{\partial \rho_{22}}{\partial t} = \hbar \left(-i\Gamma\rho_{22} + \rho_{12}\chi_1 - \rho_{21}\chi_1\right) + e^{-it\delta}\hbar\rho_{12}\chi_2 - e^{it\delta}\hbar\rho_{21}\chi_2 \tag{B.6}$$

To zero order of the probe and all orders of the pump, the solution is identical to Eq 3.3 in Section 3.1. To find the first order probe solution, we substitute the zero order solution into the master equations. To account for the population pulsation, we assume a solution for the first order density matrix so that

$$\rho_{ij}^{(1)} = a_{ij} + b_{ij}e^{i\delta t} + c_{ij}e^{-i\delta t} \tag{B.7}$$

a_{ij} is zero and by examination, the density matrix element which corresponds to the probe field is b_{12} , ie. the probe absorption is $-Im[b_{12}]$. To find b_{12}, we only need to solve one set of coupled equations

$$(\gamma - i(-\delta + \Delta))b_{12} + 2ib_{22}\chi_1 - \frac{i\Gamma\left(\gamma^2 + \Delta^2\right)\chi_2}{\Gamma\left(\gamma^2 + \Delta^2\right) + 4\gamma\chi_1^2} = 0 \tag{B.8}$$

$$(\gamma + i(\delta + \Delta))c_{21} = 2ib_{22}\chi_1 \tag{B.9}$$

$$(\Gamma + i\delta)b_{22} = \chi_1\left(-ib_{12} + ic_{21} + \frac{\Gamma(\gamma - i\Delta)\chi_2}{\Gamma\left(\gamma^2 + \Delta^2\right) + 4\gamma\chi_1^2}\right) \tag{B.10}$$

Solving for b_{12} gives

$$\frac{\Gamma(\gamma - i\Delta)\left(-(\Gamma + i\delta)(\gamma + i\Delta)(-i\gamma + \delta + \Delta) + 2\delta\chi_1^2\right)\chi_2}{\left(\Gamma\left(\gamma^2 + \Delta^2\right) + 4\gamma\chi_1^2\right)\left((\Gamma + i\delta)\left((\gamma + i\delta)^2 + \Delta^2\right) + 4(\gamma + i\delta)\chi_1^2\right)} \tag{B.11}$$